

TRADEOFFS AND EXPERIMENTAL METHODS

3.1 OCT System Tradeoffs**3.1.1 Resolution****a) Transverse resolution**

In optical coherence tomography, the transverse resolution of the image is dominated by the same Gaussian optics which limits the resolution for confocal imaging. For light of wavelength λ_0 focused on a medium of index n , the minimum focused spot size diameter d (measured at the $1/e^2$ intensity locations) is calculated as [1]:

$$d \cong \frac{2\lambda_0}{n\pi\theta}. \quad (3.1)$$

By definition, θ is the half-angle of the focused cone of light on the sample. The numerical aperture (NA) is a common parameter for defining the focusing ability of a lens, given by $NA = n \sin \theta \cong n\theta$ for small angle approximation [2].

For retinal imaging, the final focusing lens was the human eye itself. For pupil diameters smaller than 1 mm, the human eye is nearly diffraction limited. For larger pupils, aberrations distort the focused light and limit the optical performance of the lens, with varying levels of aberrations between patients. Using a pupil diameter of 1 mm, a typical human eye with a length of ~ 25 mm will have an illumination half-angle θ of:

$$\theta \cong \frac{0.5mm}{25mm} = 0.02 \text{ radians} = 1.1^\circ. \quad (3.2)$$

With an approximate refractive index of water inside the eye, this leads to a numerical aperture $NA \sim 0.027$. For a light source of wavelength $\lambda_0 = 800$ nm, using a 1 mm illumination pupil leads to a focus spot size diameter on the retina of $d = 20$ μm .

SDOCT measures reflections over a range of depths within a sample. Like confocal imaging, the transverse resolution of these measurements changes over the entire depth of the OCT image. The depth of focus is the confocal parameter which determines the depth range where the beam waist was smaller than $\sqrt{2}d$ (which is approximated as the depth region of constant transverse resolution) [3,4]. This parameter b is calculated in Gaussian optics as:

$$b = \frac{\pi d^2}{2\lambda_0}. \quad (3.3)$$

For retinal imaging in the case of $d = 20$ μm the confocal parameter b is determined to be approximately 750 μm , which is approximately the entire depth of the retina. In this case, it is expected that a SDOCT image of a human retina can be achieved with approximately uniform transverse resolution over the depth of the sample.

b) Axial/ Depth resolution

In confocal imaging, the axial resolution (also called the depth resolution) is determined by the confocal parameter. A pinhole used in conjunction with the focusing lens can improve the depth resolution further with the sacrifice of the light collection efficiency from the sample. In optical coherence tomography, the axial resolution is determined by the minimum of the coherence length l_c of the broadband light source and the confocal parameter. In most low NA scenarios such as retinal imaging, the coherence length dominates the axial resolution. In a tissue of refractive index n , the coherence length l_c describes the optical path discrimination ability, which results in an axial resolution in tissue of l_c/n .

With the ability of spectral shaping in SDOCT, the important parameter of the light source is the full spectral width, designated by $\Delta\lambda_{SOURCE}$. For a top-hat spectrum, where $\Delta\lambda_{SOURCE} = \Delta\lambda_{FWHM}$, the coherence length has been calculated as:

$$l_{C,Tophat} = 0.60 \frac{\lambda_0^2}{\Delta\lambda_{FWHM}} = 0.60 \frac{\lambda_0^2}{\Delta\lambda_{SOURCE}}. \quad (3.4)$$

For a Gaussian spectrum where $\Delta\lambda_{SOURCE} \approx 2.3\Delta\lambda_{FWHM}$ (defined by the spectral points of 3% of the maximum source power), the coherence length is:

$$l_{C,Gaussian} = 0.44 \frac{\lambda_0^2}{\Delta\lambda_{FWHM}} \approx \frac{\lambda_0^2}{\Delta\lambda_{SOURCE}}. \quad (3.5)$$

In general, the coherence length can be considered of the general form:

$$l_C = \gamma \frac{\lambda_0^2}{\Delta\lambda_{SOURCE}} \quad (3.6)$$

where $0.60 \leq \gamma \leq 1$ depends on the spectral shape of the light source.

3.1.2 System Component Tradeoffs

a) Light Source

Optical imaging of the retina of the eye is not only limited by the optical absorption of 5cm of aqueous humor in the eye, but also by the sensitivity of the photoreceptors. When two different wavelengths of light illuminate the retina with identical intensities, the wavelength at which the photoreceptors are more sensitive appears brighter to the patient and imaging with this light is more uncomfortable. The ideal wavelengths to image the retina with are in the near infrared spectral regime, where there is almost no visual response to the incoming light. Combined with the expected water absorption spectra, this leads to the ideal

wavelength choices of around 800 nm and near 1.05 μm (small absorption window in water spectrum).

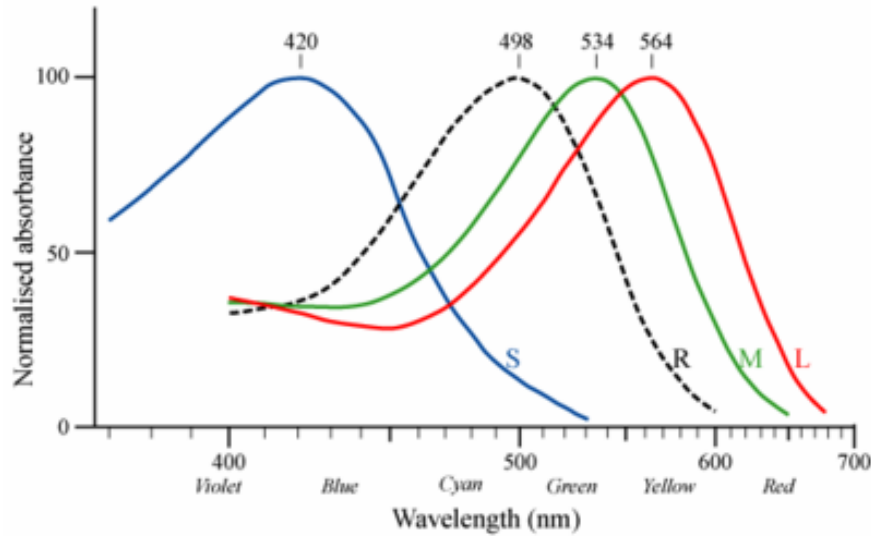


Figure 3.1: Absorption spectra of the rods (labeled R) and the three different types of cones sensitive to short (S), medium (M), and long (L) wavelengths in the retina.

With the coherence length of the form $l_c = \gamma \lambda_0^2 / \Delta \lambda_{SOURCE}$ determining the imaging axial resolution, a light source centered around 1.05 μm with a given spectral width would result in a coherence length approximately 70% larger than for the exact same spectral width around 800 nm. Two of the most important parameters of the light source for a given central wavelength are the bandwidth and the power. With an increased bandwidth, there is an increased possible axial resolution for the system. Increased light source power results in more flexibility in OCT imaging options including the system sensitivity. A source power of > 3 mW is ideal for retinal OCT imaging systems. In many cases, there is a tradeoff in light sources between bandwidth and power.

The availability of low-cost broadband light sources is the major limiting factor of achieving high-resolution OCT imaging. The highest resolution demonstrated in retinal OCT imaging utilizes a femtosecond titanium-sapphire laser [5,6]. The cost of such a laser

is typically greater than \$100,000 (more than twice the cost of the current commercial OCT imaging system) which limits the feasibility for widespread patient screening.

The most popular option for a low-cost broadband light source is a superluminescent diode (SLD), a very high power form of a light emitting diode (LED) which has been designed so that lasing does not occur. Technological developments of numerous companies have increased the selection of commercially available superluminescent diodes, with a variety of bandwidth and powers available [7].

To improve the bandwidth of the light source, multiple SLDs are commonly coupled together to produce a spectrum which is the sum of the individual SLD spectra. The limitation is that each SLD requires its own current supply and temperature controller, which multiplies the cost of the light source by the number of SLDs used. The experimental system uses a single broadband superluminescent diode to reduce the total cost of the light source. The broadest spectrum in a commercially available SLD around 800 nm has $\lambda_0=840$ nm and $\Delta\lambda_{FWHM}=50$ nm with a total source power of 16 mW (SLD-37-HP, Superlum Diodes Ltd.). The typical spectrum of this light source is plotted in Figure 3.2.

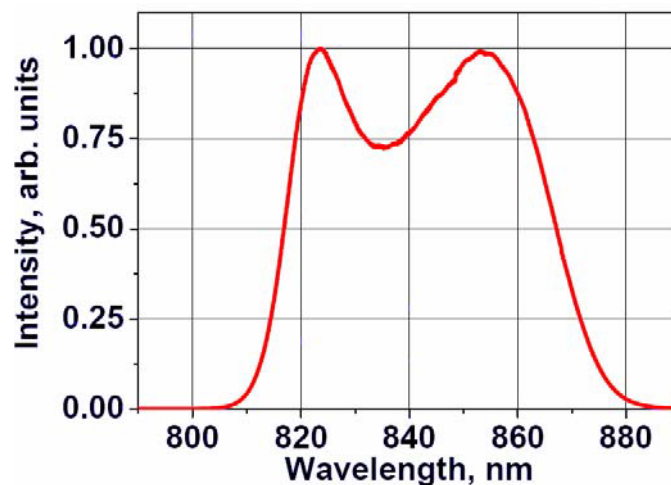


Figure 3.2: Expected spectral shape of the superluminescent diode SLD-37-HP. Image reproduced from [7].

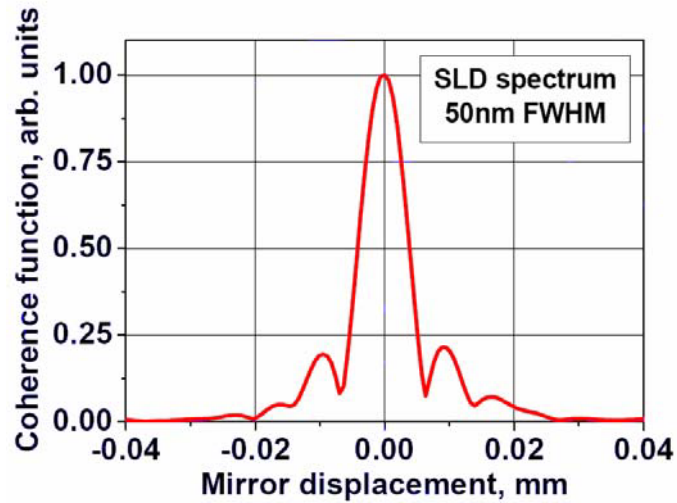


Figure 3.3: Expected coherence function for the light source of Figure 3.2. Image reproduced from [7].

With spectral shaping, the experimental light source with FWHM of 50 nm can achieve a range of coherence lengths, with a range of coherence functions as well. With a coherence length definition of $l_C = \gamma \lambda_0^2 / \Delta \lambda_{SOURCE}$, where $0.60 \leq \gamma \leq 1$ and $\Delta \lambda_{SOURCE} \approx 70$ nm for this light source, the expected coherence length range is $6.1 \mu\text{m} \leq l_C \leq 10.1 \mu\text{m}$ in air. In tissue of refractive index $n=1.38$, the coherence length in tissue is $4.4 \mu\text{m} \leq l_C / n \leq 7.3 \mu\text{m}$.

b) Fiber Optic Coupler

In the previous descriptions of the Michelson interferometer, a free space beamsplitter was used to split the incoming light into the reference and sample interferometer arms. A fiber optic coupler can accomplish the same task without requiring the same static optical alignment of the previous setup. The properties of the fiber optic coupler can be tailored to adjust the splitting ratio between the two sides of the coupler, allowing for the optimum splitting ratio to be determined.

For light of power P_0 entering the fiber optic coupler, the exiting power is split between the reference arm $((1-\eta)P_0)$ and the sample arm (ηP_0) of the interferometer. While the power

returning through the reference arm to the detector is important to determine shot noise limited operation, the power collected from the sample arm determines the system SNR performance. The power returning through the sample arm of the fiber coupler from an ideal reflector is $\rho\eta P_0$, where ρ is the geometrical coupling efficiency of the sample arm optics. The power collected from the sample arm which arrives at the detector is of the form $\rho\eta(1-\eta)P_0$, which is referred to as P_S in the SNR calculations of equation (2.47).

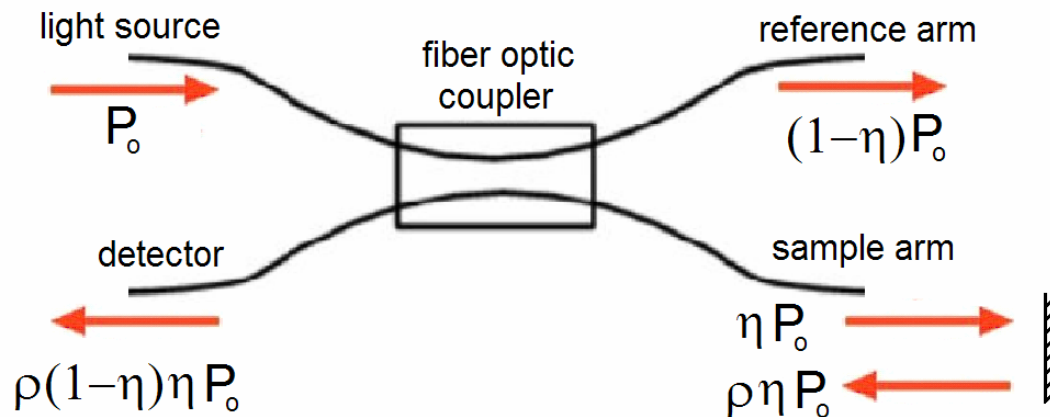


Figure 3.4: Schematic of fiber optic Michelson interferometer system with η of source power coupling into the sample arm.

As described earlier, shot noise limited SDOCT operation has a calculated SNR of:

$$\text{SNR}_{\text{SDOCT}} = \frac{\eta P_S \tau}{h \nu_0}. \quad (3.7)$$

By maximizing $P_S = \rho\eta(1-\eta)P_0$, the system performance will be improved. In general for a fixed coupling efficiency ρ , the sample power collected would be at a maximum for $\eta=0.50$ ($0 \leq \eta \leq 1$) which is the standard 50/50 coupler. This optimization is appropriate when there are no constraints on the maximum sample illumination.

The American National Standards Institute (ANSI) [8] sets limits on the maximum power exposures allowed for biomedical imaging. These restrictions protect the sample from various forms of thermal damage created from excessive energy deposition from incoming

photons. ANSI standards for retinal imaging are even more restrictive due to the added complications of possible damage to the photosensitive cells within the eye. For a light source centered about 800 nm, approximately 700 μW is allowed for constant viewing.

Retinal imaging is limited by the sample illumination power ηP_0 , so maximizing the sample power collected, $P_s = \rho(1-\eta)(\eta P_0)$ requires minimizing η . For a fixed maximum light source power P_0 , the highest efficiency occurs for a splitting factor η where ηP_0 reaches the imposed power limit or $\eta=0.5$, whichever is smaller.

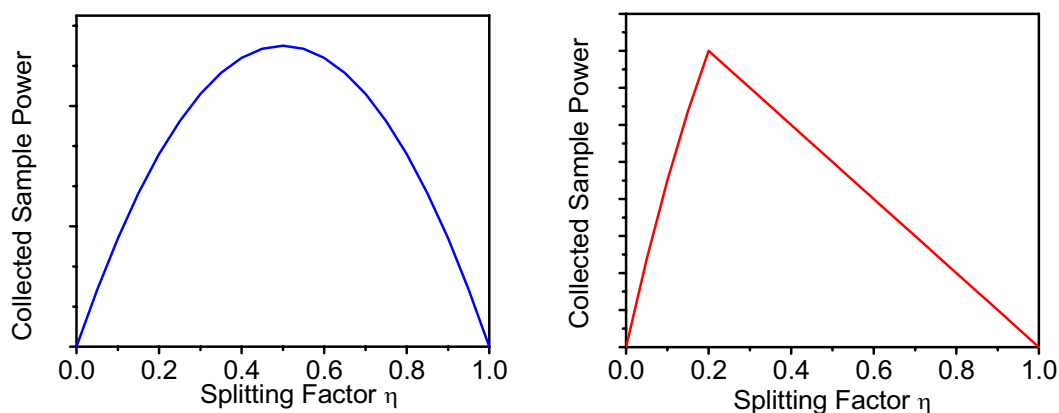


Figure 3.5: Normalized Sample Power collection versus splitting factor η for a fixed source power of P_0 with no restrictions (left) and for a case where the maximum sample power is limited to be $0.2 P_0$ (right).

3.1.3 SDOCT Specific Tradeoffs

a) Maximum A-scan rate

In SDOCT, the minimum time required to transfer the spectral data from the line scan CCD camera to the computer limits the A-scan rate of the imaging system. For the available high-speed line scan cameras, the technological limitation is the data transfer protocol Camera Link®, which transfers data from a single CCD pixel at a maximum rate of 60 MHz. For M CCD pixels acquired for each spectrometer measurement to be converted into

a single A-scan, the minimum time τ_{MIN} is given by the inverse of the maximum A-scan rate $f_{A-scan,MAX}$:

$$\tau_{MIN} = \frac{1}{f_{A-scan,MAX}} = \frac{M}{60MHz}. \quad (3.8)$$

The SDOCT system in this experiment uses $M = 2048$ in the line scan camera of the spectrometer. From this value, the minimum acquisition time and the maximum A-scan rate are calculated:

$$\tau_{MIN} = \frac{2048}{60MHz} = 34.1\mu s, \quad f_{A-scan,MAX} = 29.3 \text{ kHz}. \quad (3.9)$$

Using a 100 kHz clock rate to trigger the spectrometer acquisition, the SDOCT system uses a spectrometer read rate of 25 kHz, leading to a maximum acquisition time for the CCD pixels of 40 μs . To avoid possible crosstalk between successive spectrometer measurements, an integration time of $\tau=36.1 \mu s$ was used.

b) Tradeoffs between axial resolution and imaging depth

Previously, the coherence length was defined as $l_C = \gamma\lambda_0^2 / \Delta\lambda_{SOURCE}$ where $0.60 \leq \gamma \leq 1$ for most shapes of the light source spectrum. The maximum imaging depth of the SDOCT system was also defined as $\Delta z_{MAX} = (z_S - z_R)_{MAX} = \lambda_0^2 / 4\delta\lambda$. If we assume that the total light source spectrum is spread out over M' CCD pixels of the spectrometer (where $M' \leq M$ with M defined as the total number of CCD pixels), then

$$\Delta\lambda_{SOURCE} = M' \delta\lambda. \quad (3.10)$$

With these definitions, the relationship between the coherence length, the maximum imaging depth and the number of CCD pixels used is determined:

$$l_C = \gamma \frac{\lambda_0^2}{M' \delta\lambda} = \frac{4\gamma\Delta z_{MAX}}{M'}. \quad (3.11)$$

3.1.4 System Data Acquisition

The imaging capabilities are limited by the amount of raw data that can be handled in one acquisition. For the experimental system, each data set contains multiple spectrometer measurements, each of which contain 10-bit data acquired over 2048 CCD pixels. There are three common types of data acquisition methods for large numbers of sequential spectrometer measurements:

- i) Buffered raw data acquisition: The system memory stores all of the spectrometer data from one streamed acquisition with this option. After acquisition, the data is transferred to the computer storage for future processing and analysis. The maximum number of spectrometer measurements that can be acquired in one session is limited by the total memory (RAM) of the computer.
- ii) Data streaming to disk: This method takes the raw data from the spectrometer and transfers the information directly to the computer hard drive. If the streaming ability is faster than the data read rate of the spectrometer, the only limitation is the ultimate storage capacity of the data acquisition computer.
- iii) Real-time processing and analysis: By processing the incoming spectrometer data into OCT images, the total amount of data that needs to be stored is reduced. The ultimate limits to real-time processing depend on many factors, including the computer processor performance and the processing algorithms for the spectrometer data.

During development of analysis techniques, the ability to re-analyze previously acquired data is important. Real-time processing and analysis is useful after analysis algorithms have been finalized. To keep the cost and complexity at a minimum for this system, the buffered data acquisition method was used to acquire the spectrometer data.

The maximum number of spectrometer measurements which can be stored in system memory is approximately half of the total RAM capacity. The remaining system memory is required for the system to transfer the buffered data to disk. For 10-bit spectrometer data of

2048 individual CCD pixels, 1 GB of system RAM can buffer $256 \times 256 = 65536$ successive spectrometer scans and 2 GB of system RAM can buffer $256 \times 512 = 131072$ successive scans (which can be processed into the equivalent amount of A-scans).

3.2 Imaging Tradeoffs

Through the buffer limitations of the SDOCT system, there are a maximum number of A-scans which can be acquired in succession. Each spectrometer measurement was acquired and transferred in the time $\tau_0 = 40 \mu\text{s}$. Buffered acquisition of spectrometer data utilizes successive measurements for storage into the system memory. For 2 GB of system RAM, this translates into a total acquisition time of spectrometer data of 5.26 s, which is equivalent to 512×256 total A-scans.

Transfer of the spectrometer data from the system memory to the computer hard drive can be longer than a minute. This data transfer limits the time between sequential buffered acquisitions. To create a full 3D data set using several memory buffers of data to break up the large region of interest into parts, it is important to have a sample which is stationary enough during the data transfer time. For microscopy, many samples do not move enough within a minute to be a problem for this type of 3D image acquisition. Retinal imaging, on the other hand, suffers from numerous forms of sample motion which general increase in amplitude and frequency with acquisition time. While it is possible to perform retinal imaging using sequential buffered acquisitions to break up a 3D image into sections, it is better to optimize the data acquisition such that one memory buffer contains the entire region of interest.

To consider the transverse scan region of the 3D image, the primary transverse scan direction will be designated as x , with the secondary scan direction designated as y . The total distance scanned in each direction of the data set are given by x_{SCAN} and y_{SCAN} such that:

$$x_{SCAN} = X_{DUTY} N_X \Delta x \quad (3.12)$$

$$y_{SCAN} = N_Y \Delta y . \quad (3.13)$$

N_X and N_Y are the total number of spectrometer acquisitions used for each scan direction. The memory buffer puts the limitation $N_X N_Y \leq \sim 131072$.

X_{DUTY} describes the percentage of A-scans measured in the x-scan which are used in the 3D image. For a bi-directional scan pattern where only the scans in one direction are used for the 3D image, $X_{DUTY}=0.5$. For the same bi-directional scan where both directions are used, $X_{DUTY}=1$. Uni-directional scan patterns with fly back can tailor the duty cycle to maximize the duty cycle and optimize the buffer acquisition efficiency.

The parameters Δx and Δy describe the spatial displacement in the x and y directions between successive locations in the scan patterns. In general confocal imaging, the scan distance between different transverse locations in both the x and y directions can be chosen to be identical, such that $\Delta x = \Delta y$. In SDOCT the interferometric signal is integrated over the x-scan displacement Δx , affecting the interference fringes depending on the sample properties.

For a sample illumination beam of profile $g(x, y) \approx \exp(-4(x^2 + y^2)/d^2)$, the beam diameter d in this case is defined as the $1/e^2$ of the beam profile. Scanning across uncorrelated scatterers with this beam by a distance Δx during the spectrometer integration results in a decrease in the calculated SDOCT SNR. This decrease is of the approximate form [9]:

$$\text{SNR decrease (dB)} \approx -5 \log(1 + 0.5 \Delta x^2 / d^2) . \quad (3.14)$$

For the scan parameter choice of $\Delta x = d$ the SNR decrease is approximately -1 dB, a negligible effect on the OCT image. This decrease in SNR assumes uncorrelated scatterers, which is not always the case for samples like the human retina which contain layered structures. Constant reflecting layers are a series of correlated scatterers, and any tilt of the layer along the scan direction causes an effective axial motion to be measured. Axial

motion during spectrometer acquisition has the ability to blur interference fringes and drop the measured OCT signal considerably.

Axial motion during the integration time of the spectrometer τ can be considered as a constant velocity in the z-direction v_z . In this case, the interference fringe signal which is measured in k-space is of the form:

$$P(k) \propto \int_0^{\tau} \cos(2k(z_0' + v_z t)) dt = \frac{1}{v_z} \int_{z_0 - \Delta z/2}^{z_0 + \Delta z/2} \cos(2kz) dz . \quad (3.15)$$

In this case, the axial motion during the integration time was $\Delta z = v_z \tau$. For no motion, the interference signal $P(k) \propto \cos(2kz_0) = P_0$. In general, the normalized interference power measured is:

$$\frac{P(k)}{P_0} = \frac{\sin(k\Delta z)}{k\Delta z} . \quad (3.16)$$

This results in a normalized OCT intensity:

$$\left(\frac{I}{I_0} \right)^2 = \left(\frac{\sin(k_0 \Delta z)}{k_0 \Delta z} \right)^2 . \quad (3.17)$$

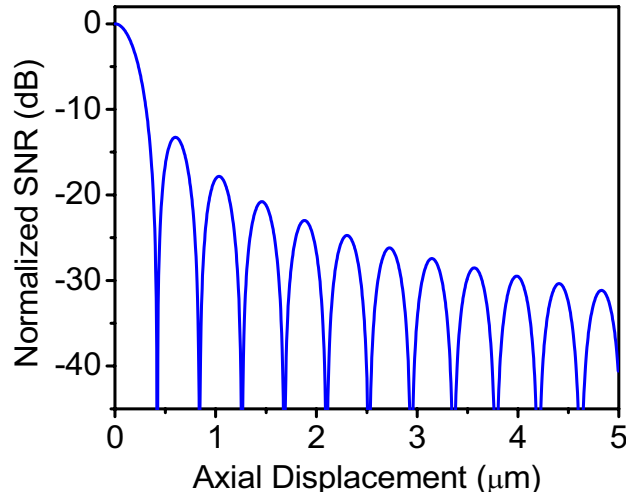


Figure 3.6: Normalized OCT intensity signal in logarithmic scale as a function of the axial motion which occurs during the spectrometer integration time. Center wavelength of 840 nm used for calculation.

The first minimum in this function $(I/I_0)^2 = 0$ occurs when $k_0\Delta z = \pi$, which results in $\Delta z = \lambda_0/2$. For a x-scan displacement of Δx , there is a maximum tilt angle of a correlated layer which can be measured before $(I/I_0)^2 = 0$. Defining a tilt angle θ such that $\theta = 0^\circ$ for a horizontal layer, the maximum transverse scan before the OCT signal is completely blurred out for a layer of a given tilt θ is calculated to be:

$$\Delta x = \frac{\lambda_0/2}{\tan \theta}. \quad (3.18)$$

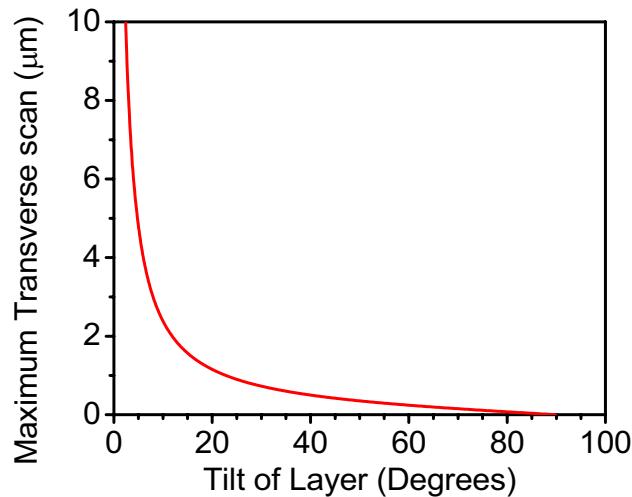


Figure 3.7: Minimum transverse scan Δx required to completely remove the OCT signal for a given tilt of a correlated scatterer layer.

The maximum transverse scan for a given tilt angle is independent of the diameter of the illumination beam. This is adequate for high transverse resolution scenarios such as microscopy, but seriously limits low transverse resolution situations such as retinal imaging. To reduce these issues, a high-density scan along the x-direction chosen such that $\Delta x \ll d$ is generally employed.

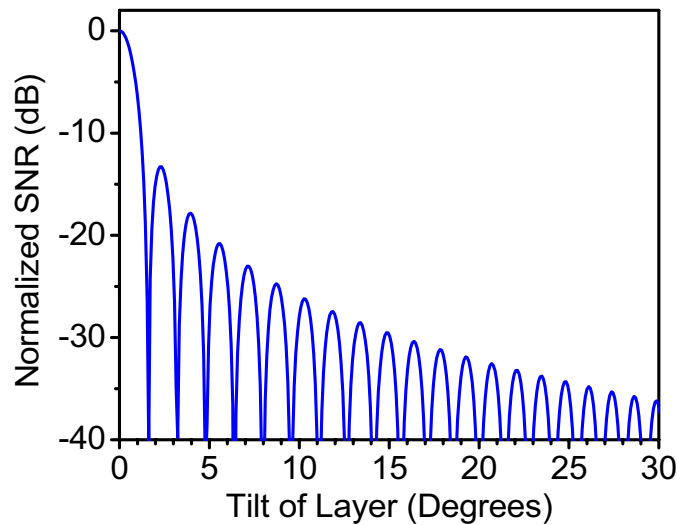


Figure 3.8: Normalized OCT intensity signal as a function of tilt angle for a transverse scan $\Delta x = 15 \mu\text{m}$.

For a transverse scan size of 15 mm, a comparable size to the transverse resolution experienced in retinal imaging, the OCT signal measured depends heavily on the tilt and correlation of the scatterer layers in the eye.

3.3 Phase Contrast Tradeoffs

The phase change measured for a given depth z with a time separation T , designated as $\Delta\phi(z,T)$, has a combination of several factors affecting the accuracy of the measurement:

$$\Delta\phi(z,T) = \Delta\phi_{\text{scatterer}}(z,T) + \Delta\phi_{\text{bulk}}(T) + \Delta\phi_{\text{SNR}}(z) + \Delta\phi_{\text{error,other}}(T). \quad (3.19)$$

The motion of interest is from the scatterers located at the depth z , referred to as the phase change term $\Delta\phi_{\text{scatterer}}(z,T)$. The total phase change $\Delta\phi(z,T)$ also contains the bulk motion of the entire sample along the imaging (axial) direction $\Delta\phi_{\text{bulk}}(T)$, caused by relative phase motion between the sample and the system and ideally is independent of depth z of the scatterers. $\Delta\phi_{\text{SNR}}(z)$ designates a phase error associated with the local SNR of the data calculated at the depth z and is independent of time for a constant SNR. Experimental and

theoretical results have determined that the standard deviation of SNR-limited phase error for phase changes has the form of equation 2.64 [10,11]:

$$\sigma_{\Delta\phi, \text{SNR}}(z) = \frac{1}{\sqrt{\text{SNR}(z)}}. \quad (3.20)$$

$\Delta\phi_{\text{error,other}}(z,T)$ encompasses the other phase errors which may occur for SDOCT phase measurements, including but not limited to phase changes caused by transverse motion across a scatterer at depth z , artifacts associated with limited depth sampling during axial motion of the sample or other computational based phase anomalies. By understanding the effects $\Delta\phi_{\text{bulk}}(T)$, $\Delta\phi_{\text{SNR}}(z)$, and $\Delta\phi_{\text{error,other}}(z,T)$ have on the accuracy of phase measurements in a SDOCT system, improvements can be made to reduce the adverse effects of these terms in the phase contrast images.

3.3.1 Doppler Flow Contrast

The phase change measured for a given reflection with a time separation T , defined as $\Delta\phi(T)$, corresponds to the net axial motion which has occurred during the time T . Observing flow of velocity v , oriented at an angle θ from the horizontal (in the case of the interferometer light arriving vertically upon the sample) results in the phase measurement proportional to the flow component along the imaging direction, designated as v_z [12,13]:

$$\Delta z(T) = \frac{\lambda_0}{4\pi} \Delta\phi(T) = v_z T = v T \sin \theta. \quad (3.21)$$

There are limits to the calculation of the axial flow component using the mean phase change of the scatterers. With the phase determined within a range of 2π , there is a limit to the maximum phase change that can be determined due to phase wrapping. Phase wrapping is created by the cyclic nature of the phase measurement. With phase determined from 0 to 2π , any phase change from $0 \rightarrow -\delta\phi$ appears as $0 \rightarrow 2\pi - \delta\phi$. This effect limits the maximum discernable phase change as $\Delta\phi_{\text{MAX}} = \pm\pi$. Using the minimum possible time

separation of phase changes $T=\tau_0=40\mu\text{s}$, the maximum possible axial velocity component that can be calculated in a medium of refractive index $n=1.35$ is:

$$v_{Z,MAX} = \frac{\Delta z_{MAX}}{\tau_0} = \frac{\lambda_0}{4\pi n} \frac{\Delta\phi_{MAX}}{\tau_0} = \pm \frac{\lambda_0}{4\tau_0} = \pm 3.9\text{mm/s.} \quad (3.22)$$

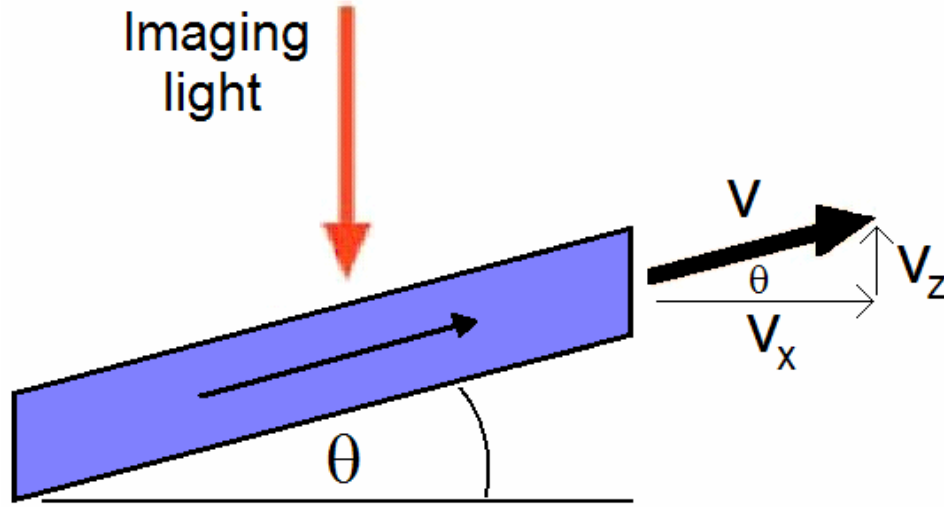


Figure 3.9: Schematic of flow measurement alignment for Doppler flow contrast.

The minimum possible velocity that can be identified is determined by the SNR-limited phase error of the OCT image. For a general Doppler image, assume that the maximum phase variance error in the image $\sigma_{\Delta\phi,MAX}$ determines the minimum observable axial flow. In that case set $\sigma_{\Delta\phi,MAX}=1$, which corresponds to $\text{SNR}(z)=1$ for the image. For N averages of the phase change measurements, the phase error measured reduces to $\sigma_{\Delta\phi,MAX}/\sqrt{N}=1/\sqrt{N}$ for the above assumption. For the minimum time separation $T=\tau_0$ of N phase changes, the minimum measurable axial velocity is:

$$v_{Z,MAX} = \frac{\lambda_0}{4\pi n \tau_0} \frac{\sigma_{\Delta\phi,MAX}}{\sqrt{N}} = \frac{1.23\text{mm/s}}{\sqrt{N}}. \quad (3.23)$$

With the axial flow component defined as $v_z = v \sin \theta$, visualization of flow is very difficult when the flow is slow or oriented horizontally such that $\theta \sim 0^\circ$. With an increased time separation T between phase measurements, the minimum and maximum axial velocities that can be quantitatively measured are reduced. This improves the minimum velocity visualization while hindering the faster flow imaging. Different analysis of the phase information has the potential of improving on the visualization abilities of the Doppler flow technique, allowing for visualizing slow and horizontal flows as well as the fastest flows in the system.

3.3.2 Phase Variance Contrast

Variance is another statistical analysis tool which looks at different properties of the data. While the average phase change describes the net axial motion occurring during the imaging time, the variance of the phase deals with the fluctuations in the measured motion. The variance of the phase changes $\Delta\phi(z,T)$ for scatterers at a depth z with a time separation T is calculated using the form of the statistical variance:

$$\sigma_{\Delta\phi}^2(z,T) = \langle \Delta\phi(z,T)^2 \rangle - \langle \Delta\phi(z,T) \rangle^2. \quad (3.24)$$

Assuming no correlation between the different phase factors which compose the phase change measured in equation 3.20, the variance of the phase changes can be calculated as the summation of the variances of the individual components:

$$\sigma_{\Delta\phi}^2(z,T) = \sigma_{\Delta\phi,scatterer}^2(z,T) + \sigma_{\Delta\phi,bulk}^2(T) + \sigma_{\Delta\phi,SNR}^2(z) + \sigma_{error,other}^2(z). \quad (3.25)$$

The primary source of motion contrast in this variance calculation is $\sigma_{\Delta\phi,scatterer}^2(z,T)$, which in general depends on the time separation T of the phase changes. $\sigma_{\Delta\phi,bulk}^2(T)$ describes the variance of the bulk axial motion of the sample for time separations T over the imaging time. For extremely stable imaging scenarios, this factor is not a major consideration. The phase error due to SNR limitations $\sigma_{\Delta\phi,SNR}^2(z)$ for a given depth z has been described previously in equation 3.21. One factor to note is the time independence of this factor,

assuming approximately constant OCT signal over the total imaging time. All of the other possible phase error sources are encompassed into one term $\sigma_{\text{error,other}}^2(z)$ for current analysis purposes.

There are four types of motion which contain components that are observable through the variance measurement of the phase motion:

- Variations in the axial component of flow
- Transverse flow effects of uncorrelated scatterers
- Axial component of Brownian-type random motion
- Ensemble statistical effects of uncorrelated scatterers

To understand the expected form of the motion variance, each of these scenarios must be individually analyzed. For adequate contrast to be observed, imaging parameters must be chosen such that the phase variance measured from the above-mentioned motion surpasses the variance limitations imposed by the SNR-limited phase error and the other phase noise factors.

3.3.3 Variations in Axial Flow

In situations containing flow, the macroscopic flow determination describes the mean flow from all the individual particles which compose the flowing media. It is typical to expect the flow from a given particle to experience flow variations from the measured mean flow. Collisions between flowing particles, variations in directionality of an individual particle's motion, or interference with static barriers at the edge of the flow region are all possible sources of flow variations within an ensemble of flowing particles.

For this analysis, assume that the distribution of velocities is independent in time. Define the distribution to have a mean axial velocity of v_z and a standard deviation of σ_{v_z} . Using

a time between phase measurements of T , the calculated standard deviation of the phase changes is determined as:

$$\sigma_{\Delta\phi}(T) = \frac{4\pi n \sigma_{vz} T}{\lambda_0}. \quad (3.26)$$

Using $T = \beta\tau_0$ and requiring $\sigma_{\Delta\phi}(T) > 1$ to create contrast beyond the SNR-limited phase error, the axial velocity variation able to produce contrast in a tissue of index $n=1.35$ is:

$$\sigma_{vz} > \frac{\lambda_0}{4\pi n T} = \frac{1.23 \text{ mm/s}}{\beta}. \quad (3.27)$$

While a large variation is required for phase measurements between sequential A-scans such that $\beta=1$, for the case of $\beta=250$ the required variation drops down to $\sigma_{vz} > 5 \mu\text{m/s}$.

3.3.4 Transverse Flow Effects

B. Park et al. [14] theoretically calculated and experimentally measured the error of phase change measurements of uncorrelated scatterers when the two phase measurements were taken at different transverse locations. The intention of this work was to determine the limitations of Doppler flow imaging while scanning transversely across a sample. Using a Gaussian beam with a $1/e^2$ beam width = d at the focus, the standard deviation of the phase changes was determined for a transverse scan of the beam Δx between A-scans. Defining the fraction of the beam width as $\Delta x/d$, the variance of the phase error due to the transverse motion was calculated to be:

$$\sigma^2_{\Delta\phi} = \frac{4\pi}{3} \left(1 - \exp\left(-2\left(\frac{\Delta x}{d}\right)^2\right) \right). \quad (3.28)$$

The functional form of this phase error calculation was verified through experimental measurements. For very small transverse motions, the phase error is dominated by the SNR-limited phase error (described by the horizontal dotted line on Figure 3.10) as

expected. For transverse motions of approximately the full beam width d , the experimental phase error was lower than theoretically predicted. This discrepancy is caused by the limitations imposed on the maximum phase change measured in the SDOCT system of $\pm\pi$. For a completely random distribution of phase changes, the expected phase error is $\sigma_{\Delta\phi} = 1.815$ radians, which gives a phase variance of $\sigma^2_{\Delta\phi} = 3.29$ radians². This maximum phase error is consistent with the experimental data of the paper.

The theory of the phase error during transverse scanning only assumes a relative transverse motion between the sample illumination light and the sample. If the scanning beam is held stationary, any transverse flow of uncorrelated scatterers would provide the same relative transverse motion. This allows motion contrast to be observed in transverse flow regions and no contrast to be observed in the other regions of the static sample.

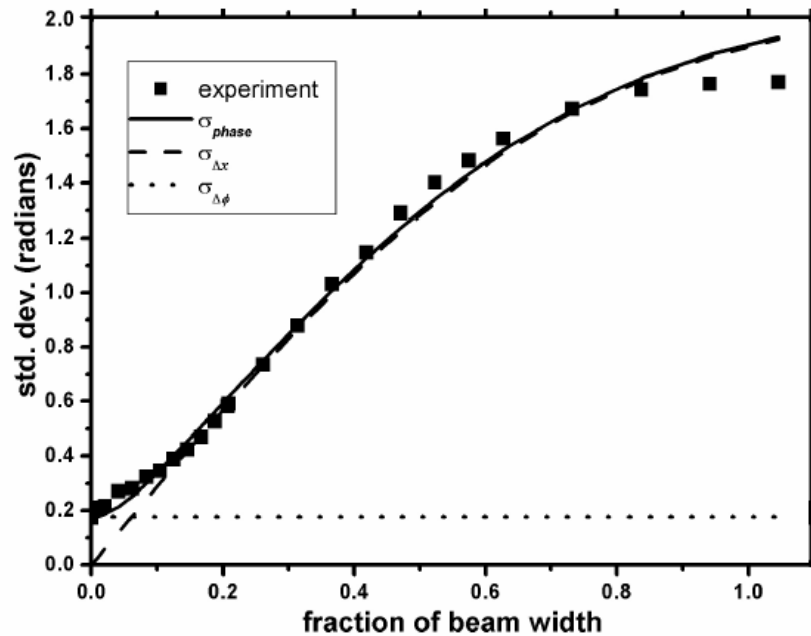


Figure 3.10: Experimentally measured phase change errors as a function of the transverse displacement between A-scans. Theoretical phase error estimates are also plotted. Data reproduced from [14].

Using the previously determined phase error form, the phase variance contrast $\sigma^2_{\Delta\phi} = 1$ occurs for the case of $\Delta x / d = 0.37$. Using the same flow terminology as described earlier,

the transverse displacement caused by the flow within a time T for a velocity v oriented at an angle θ to the horizontal is:

$$\Delta x(T) = v_x T = v T \cos \theta. \quad (3.29)$$

For the phase variance contrast $\sigma^2_{\Delta\phi} > 1$ case using $d = d_0 \times 10^{-6}$ m and $T = \beta\tau_0 = \beta \times 40\mu\text{s}$, the conditions for contrast are:

$$\frac{\Delta x(T)}{d} = \frac{v_x T}{d} > 0.37 \quad (3.30)$$

$$v_x > 9.25 \frac{d_0}{\beta} \text{ mm/s}. \quad (3.31)$$

This form of variance contrast is the only one which depends on the diameter of the focused light on the sample. For retinal imaging cases where $d=20 \mu\text{m}$, sequential A-scans such that $\beta=1$ requires a substantial transverse velocity $> 185 \text{ mm/s}$ to be visualized due to this form of contrast. For the case of $\beta=250$, the required velocity component reduces to $v_x > 0.74 \text{ mm/s}$.

Comparing the phase variance contrasts due to flow can determine the dominant process for various flow velocities and angles. Each of the lines plot the minimum velocity required for a given flow angle to achieve phase variance contrast from the motion. For the case of retinal imaging, let the focus spot diameter $d=20 \mu\text{m}$. The blue line is the minimum velocity to observe transverse flow phase variance effects. For graphical representation, it is assumed that the variance of the velocity distribution is a percentage of the mean velocity. The minimum velocity required to view phase variance contrast is plotted in the cases where the velocity variance is 1% (red line) and 10% (green line) of the total mean velocity. The velocity regimes were examined in Figure 3.11 for different time separations T of the phase change, in the cases where $\beta=1$ ($T=40 \mu\text{s}$), $\beta=25$ ($T=1 \text{ ms}$) and $\beta=250$ ($T=10 \text{ ms}$).

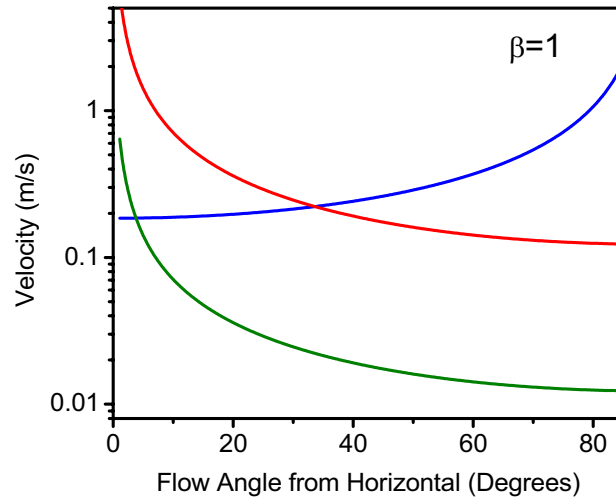


Figure 3.11 a): Minimum flow velocity required to demonstrate phase variance contrast in three different scenarios of transverse flow and axial flow variance. The time between phase measurements is $40 \mu\text{s}$ for this estimate.

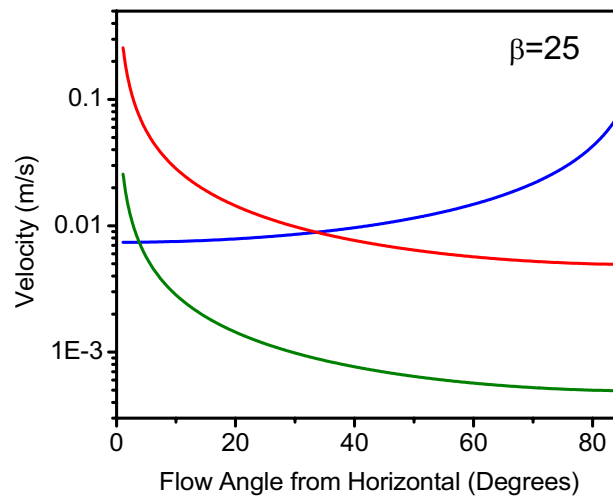


Figure 3.11 b): Minimum flow velocity required to demonstrate phase variance contrast in three different scenarios of transverse flow and axial flow variance. The time between phase measurements is 1 ms for this estimate.

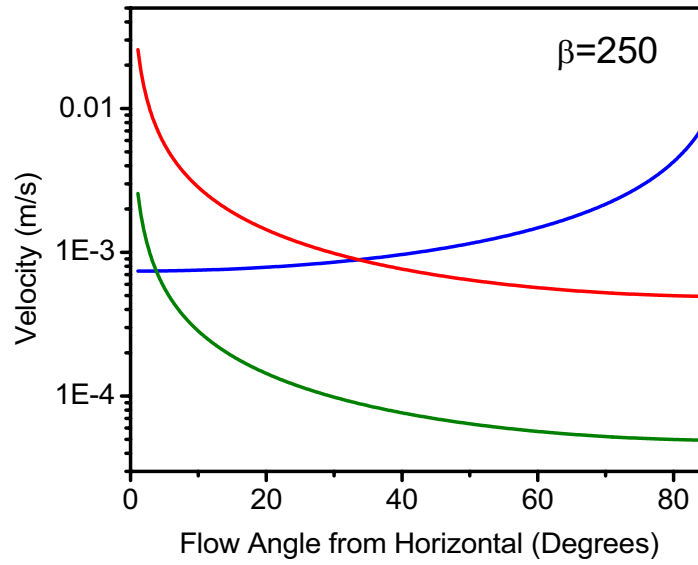


Figure 3.11 c): Minimum flow velocity required to demonstrate phase variance contrast in three different scenarios of transverse flow and axial flow variance. The time between phase measurements is 10 ms for this estimate.

With the fact that most of the retinal vessels lie nearly horizontal, perpendicular to the imaging direction, the phase effects due to transverse flow become the most dominant. For cases in which the velocity distributions have a variance $> 10\%$ of the mean velocity, the axial flow variations become just as important, assuming that $\theta \neq 0^\circ$.

3.3.5 Axial Component of Brownian Motion

The random motion of diffusion spheres, referred to as Brownian motion, is caused by the thermal fluctuations of the mobile scatterers. While the net motion along any direction is zero, the variance of the motion is a measurable quantity which increases with time between position measurements T . Assuming an isotropic scenario where the scatterers can move freely in all directions, the variance of motion along the axial direction $\sigma_{\Delta z}^2(T) = \langle (\Delta z)^2 \rangle$ is one third of the total diffusive motion variance $\langle (\Delta r)^2 \rangle$. The transverse motion creates an effective axial motion as described by equation (3.28), with a variance defined as

$\sigma_{\Delta z, \text{eff}}^2(T)$. The axial motion variance and the effective axial motion variance for a focused illumination beam diameter d are described by the diffusion constant D of the form [15]:

$$\sigma_{\Delta z}^2(T) = \langle (\Delta z)^2 \rangle = \frac{1}{3} \langle (\Delta r)^2 \rangle = \frac{D T}{3} = \frac{E_B}{3\pi\eta r} T$$

$$\sigma_{\Delta z, \text{eff}}^2(T) \cong \frac{1}{3\pi} \left(\frac{\lambda}{d} \right)^2 \sigma_{\Delta z}^2(T) \quad (3.32)$$

For most OCT imaging systems, the beam diameter is large enough that the effective axial motion caused by the transverse Brownian motion is negligible. In the definition of the diffusion constant, E_B is the thermal energy term which is calculated using the Boltzmann constant times the temperature $E_B = k_B T_{TEMP}$. The term η describes the viscosity of the media in which the scatterers are moving. The last term r is the radius of the spheres undergoing the thermal motion. For the case of room temperature water, $E_B = k_B T_{TEMP} = 4.04 \times 10^{-21}$ J and $\eta = 1.00 \times 10^{-3}$ Pa-sec. Defining the radius $r = r_0 \times 10^{-6}$ m and the time $T = \beta \tau_0 = \beta \times 40$ μ s, The expected motion is:

$$\sigma_{\Delta z}(T) = \sqrt{\frac{E_B}{3\pi\eta r} T} = 4.1 \sqrt{\frac{\beta}{r_0}} \text{ nm.} \quad (3.33)$$

For the same phase contrast requirement used earlier $\sigma_{\Delta\phi}(T) = (4\pi m / \lambda_0) \sigma_{\Delta z}(T) > 1$ radian, the parameters required to visualize Brownian motion are determined:

$$\frac{\beta}{r_0} > 146. \quad (3.34)$$

In this case, spheres of radius 1 μ m require phase changes with time separations of > 5.8 ms to see substantial motion contrast. This approximate parameter determination assumes free scatterers in room-temperature water. Different media and non-isotropic diffusion will require different imaging times to adequately visualize contrast.

3.3.6 Ensemble Phase Effects

All of the OCT analysis so far has assumed interference from a single reflector for a given depth within the sample. In reality, due to the finite size of the imaging voxel (the three dimensional spatial extent which defines the volumetric OCT resolution) there can exist multiple reflectors inside of one of them. The volume of a voxel can be approximated as $V = l_c d^2$, where l_c is the coherence length of the imaging system and d is the $1/e^2$ diameter of the focused light at the given depth. With the large d associated with retinal imaging, there is an increased possibility of multiple scatterers residing within one voxel.

Multiple scatterers within a voxel each have their own interference signal $\tilde{R}_j = R_j \exp(i\phi_j)$. The measured OCT interference signal is the summation of all of the individual scatterers within the voxel of interest:

$$\tilde{S} = S \exp(i\phi_s) = \sum_j \tilde{R}_j = \sum_j R_j \exp(i\phi_j). \quad (3.35)$$

Correlated scatterers are static reflections with fixed distances between all of the scatterers. For the case of correlated scatterers within the voxel, the resulting measured interferometric signal appears the same as if there was a single reflector. Uncorrelated scatterers are independent of each other in terms of relative distance and motion and reflection intensity. The phase measured for a voxel containing uncorrelated scatterers varies dynamically with the properties of the individual particles.

Consider the case of two identical scatterers located within a given voxel with a fixed distance between them. Let the maximum reflection for each of the scatterers be defined equally as $R_{1,MAX} = R_{2,MAX} = R_0$.

Let the reflections for each of the scatterers be defined as a time-varying function $R_j(t) = R_0 g_j(t)$, where $g_j(t)$ is a random distribution from zero to one which is independent of j . This function describes the percentage of reflected light directed towards the interferometer arm for collection. If we define the special case of the scatterer

separation distance such that the phase difference is given by π , the measured interferometric signal is of the form:

$$\begin{aligned}\tilde{S} &= S \exp(i\phi_S) = \sum_j \tilde{R}_j = R_1(t) \exp(i\phi_1) + R_2(t) \exp(i\phi_2) \\ &= R_0(g_1(t) - g_2(t)) \exp(i\phi_1).\end{aligned}\quad (3.36)$$

With the requirement of $S > 0$, the calculated phase of the interferometric signal ϕ_S is ϕ_1 for the case of $g_1(t) - g_2(t) > 0$ and $-\pi + \phi_1$ for the case of $g_1(t) - g_2(t) < 0$.

With $g_1(t)$ and $g_2(t)$ describing independent random distributions of equal magnitude, there exists an equal probability of measuring a phase of ϕ_1 as $-\pi + \phi_1$. Therefore half of the measured phase changes = 0 and the other half would be split evenly between $-\pi$ and π . The resulting calculation for the variance of the phase change is given by:

$$\begin{aligned}\sigma_{\Delta\phi}^2(z, T) &= \langle \Delta\phi(z, T)^2 \rangle - \langle \Delta\phi(z, T) \rangle^2 \\ \langle \Delta\phi \rangle &= \frac{1}{2}(0) + \frac{1}{4}(\pi) + \frac{1}{4}(-\pi) = 0 \\ \langle \Delta\phi^2 \rangle &= \frac{1}{2}(0) + \frac{1}{4}(\pi^2) + \frac{1}{4}(\pi^2) = \frac{\pi^2}{2} \\ \sigma_{\Delta\phi}^2 &= \frac{\pi^2}{2} \neq 0.\end{aligned}\quad (3.37)$$

It is important to note that the mean phase change measured, which is associated with the Doppler flow measurement, is zero. On the other hand, the phase change variance calculated for this case is not zero.

In reality, the function $g_j(t)$ would not be completely random for short time changes but could be completely random for larger time separations. Also the probability is that these scatterers would be undergoing motion as well which would need to be considered. Regardless, for more scatterers, phase differences not equal to π , and non-stationary

scatterers the variance calculation becomes much more complicated (but will not be zero in general).

3.4 Phase Contrast Method: MB-Scan

In each of the forms of phase variance presented, the magnitude of the variance increases with the time separation between phase measurements. To maximize the phase contrast capabilities for measuring the motion variance, phase changes should be measured for time separations much larger than the readout time τ_0 of the spectrometer. The simplest way to acquire this phase information is to wait at a given transverse location, taking A-scans until enough phase information has been acquired before moving to the next location. By repeating this process over multiple transverse positions, a two-dimensional phase contrast image can be created.

The scan terminology used in optical coherence tomography was developed for ultrasound applications. Each depth scan of the interference fringe information, which corresponds to one measurement of the spectrometer data, is called an A-scan. The process of waiting at one transverse location, collecting multiple A-scans over time is referred to as an M-scan. Acquiring multiple A-scans over different transverse locations creates a B-scan, a two dimensional cross-sectional reflectivity image of the sample. For the work presented, the process of using multiple M-scans over different transverse locations to create a two-dimensional phase contrast image will be referred to as an MB-scan.

3.4.1 Varying MB-Scan Imaging Parameters

To determine the limitations of producing a contrast image, a test case was created capable of producing phase variance motion. An Intralipid solution was used to fill the molded wells created from agarose, a gelatin-like material. The Intralipid solution was diluted to approximately match the OCT intensity signal from the agarose, reducing the contrast between the regions observed within the intensity image. For 2% agarose wells, an Intralipid solution of approximately 0.1% was used to match the intensity image. Zooming

in on a single B-scan of the Intralipid-filled agarose wells, it is very difficult to identify the material occupying each region of the image.

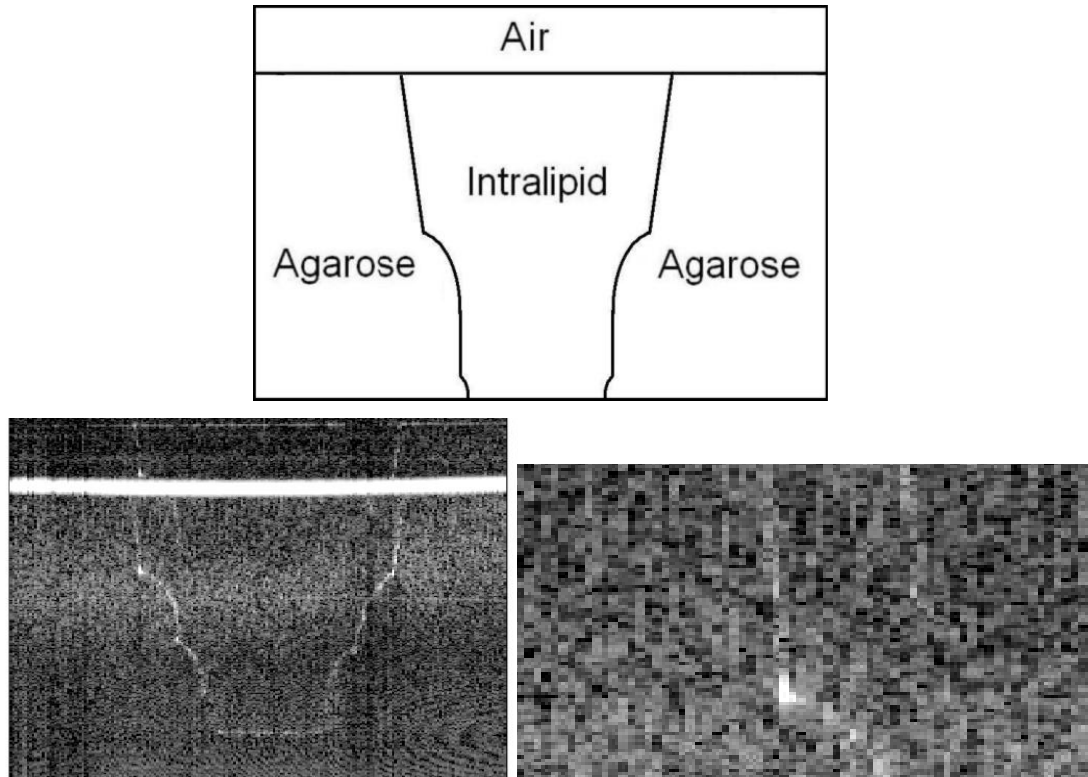


Figure 3.12: 2% Agarose well filled with intensity-matched 0.1% Intralipid solution. The schematic of the sample (top) corresponds with the non-averaged OCT intensity image (left). The zoomed-in portion of the intensity image (right) demonstrates the lack of intensity contrast within this image.

The static agarose is expected to produce no motion contrast while the Intralipid solution is expected to demonstrate Brownian motion. Some of the effects of the motion can be observed through the averaged OCT intensity image, created from 200 A-scans at each transverse location. During the imaging time, the Intralipid scatterers have moved enough to homogenize a region of the image which looked granular before averaging occurred. Textural differentiation of regions is not a new concept in OCT [16], but it usually requires large regions of the image to be effective. Phase variance does not have these spatial requirements to create contrast in images.

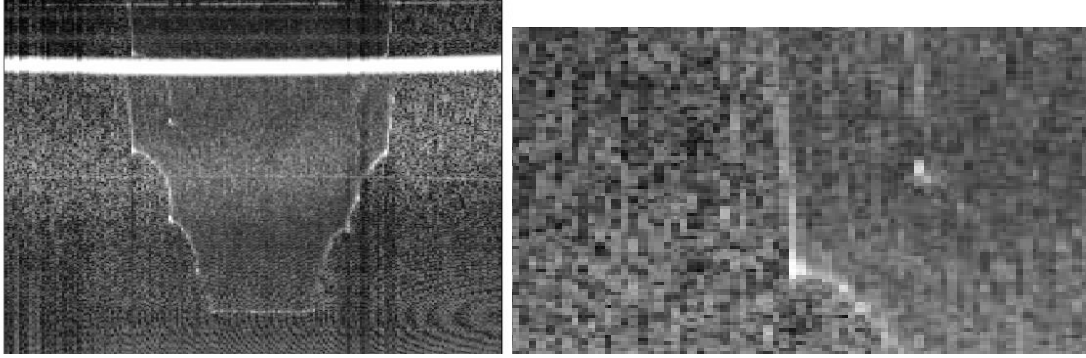


Figure 3.13: 2% Agarose well filled with intensity-matched 0.1% Intralipid solution. The averaged OCT intensity image (left) and the zoomed-in portion of the image (right) can observe textural changes between the two mobility regions.

The phase variance for phase changes separated by time $T = \beta\tau_0$ for a depth z for the agarose/Intralipid sample is of the form:

$$\sigma_{\Delta\phi}^2(z, T) = \sigma_{\Delta\phi, \text{scatterer}}^2(z, T) + \sigma_{\Delta\phi, \text{bulk}}^2(T) + \sigma_{\Delta\phi, \text{SNR}}^2(z). \quad (3.38)$$

From the previous derivations, the motion variance of the scatterers $\sigma_{\Delta\phi, \text{scatterer}}^2(z, T)$ is expected to increase with larger time separations while the SNR-limited phase noise $\sigma_{\Delta\phi, \text{SNR}}^2(z)$ is expected to remain constant over time. One assumption of these measurements is that for most short-time separations, the bulk motion will be small enough to have $\sigma_{\Delta\phi, \text{bulk}}^2(T)$ be considered negligible. This assumption can be tested through the phase variance measurement of the air/water interface of the OCT image, which is expected to have very low values of motion and SNR-limited phase error. Any significant uncorrected bulk motion during the analyzed A-scans will appear in the phase variance measured for that interface.

Using the SDOCT system with the sample arm of the interferometer set up for microscopy with an approximate transverse resolution of $d = 5 \mu\text{m}$, an MB-scan was acquired for 200 transverse locations extending over 1.6 mm, with each location containing 200 sequential A-scans. The entire data set was acquired in 1.6 s total time. For all of the phase data over time acquired for the image, the phase variance was calculated for each image pixel by using all of the phase changes for A-scans separated in time by $T = \beta\tau_0$. By increasing the time between phase measurements, the total number of phase changes that can be acquired

from 200 A-scans for one pixel is reduced as well. For 200 A-scans composing each M-scan, the phase variance image was calculated for time separations ranging from $T = \tau_0 = 40 \mu\text{s}$ to $T = 40\tau_0 = 1.6 \text{ ms}$. All of the presented images are dimensionally scaled and cropped to highlight the region of interest. The image scale for the variance images is a phase variance range of 0 to 2 radians².

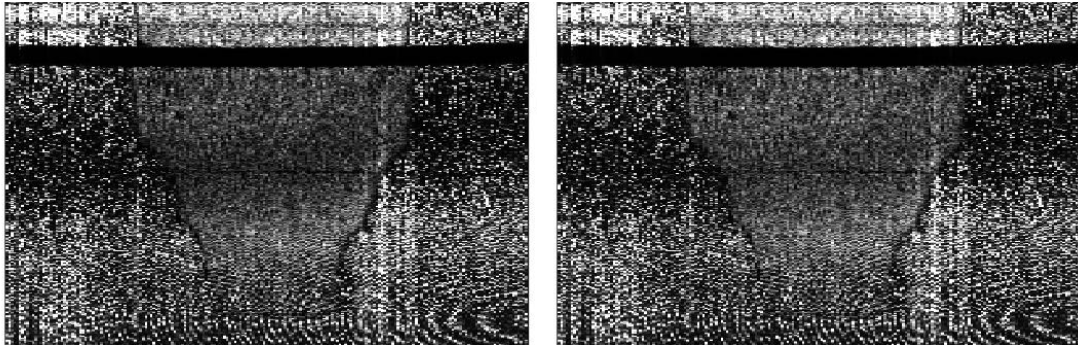


Figure 3.14 a): Phase variance images for phase change time separations $T = 40 \mu\text{s}$ (left) and $T = 80 \mu\text{s}$ (right).

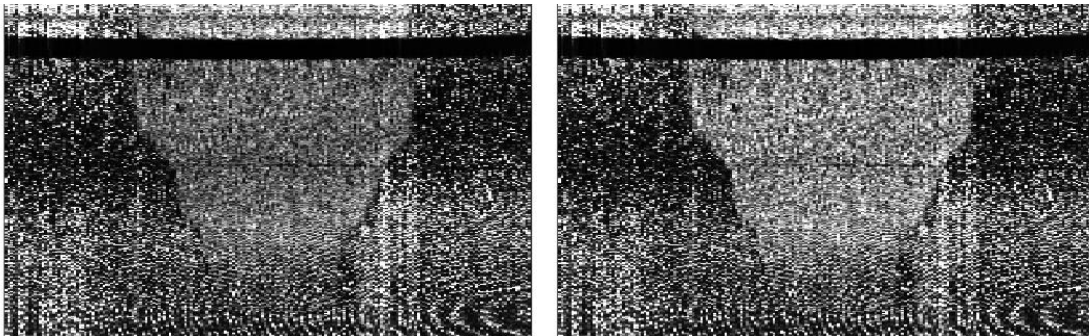


Figure 3.14 b): Phase variance images for phase change time separations $T = 200 \mu\text{s}$ (left) and $T = 400 \mu\text{s}$ (right).

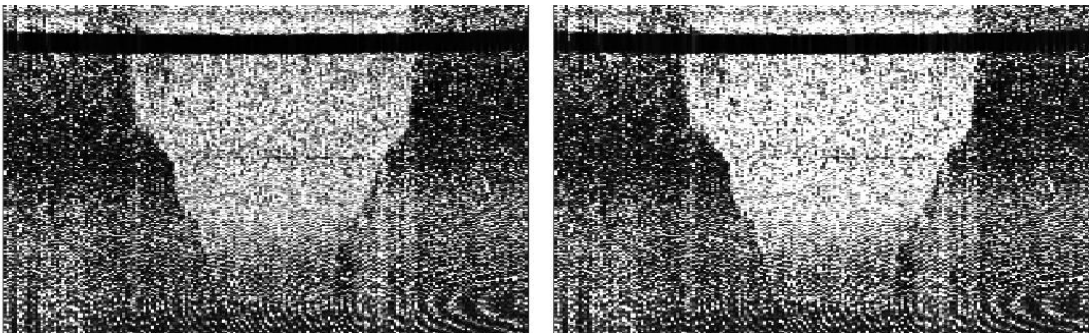


Figure 3.14 c): Phase variance images for phase change time separations $T = 800 \mu\text{s}$ (left) and $T = 1.6 \text{ ms}$ (right).

While the phase variance increased with time as expected, phase contrast can still be observed in all of the cases including the quickest $T = 40 \mu\text{s}$ case. This visualization is courtesy of the significant statistics used for creating the phase variance calculations. Even in the $T = 40 \mu\text{s}$ case, phase changes measured from successive A-scans used all 200 A-scans to create the phase variance (a total M-scan time of 8 ms). By reducing the total amount of statistics used to create the phase variance image, the contrast between the different regions is reduced.

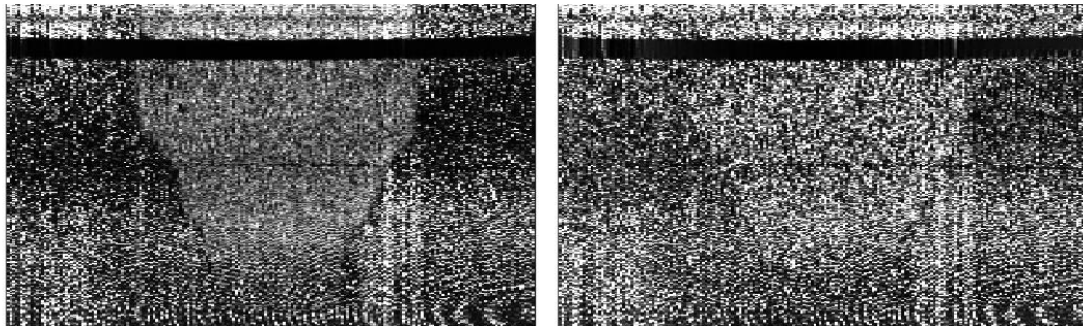


Figure 3.15: Comparing the effect of statistics on the phase variance image for time separations of $T=5\tau_0=200 \mu\text{s}$. The total number of A-scans used for statistics is 200 (left) and 30 (right). The total time to acquire the data required to create each of these images is 1.6 s (left) and 0.24 s (right).

Reducing statistics used for contrast imaging is important to optimize the buffered acquisition of the SDOCT system. The presented MB-scan contains 40,000 total A-scans, with 200 A-scans at each of 200 transverse locations. With a maximum buffer size of approximately 130,000 A-scans, the MB-scan in the current form is not a feasible option for 3D phase contrast imaging. To optimize the acquisition size of the data required to construct a 2D phase contrast image, the time between phase measurements must be reduced along with the total number of statistics. This will help determine the ideal time separations required to visualize the Brownian motion in this sample.

The major factor limiting contrast in the above images is the SNR phase error, which is independent of the time separation used for the phase variance calculations. With access to all of the phase information measured during the MB-scan, the phase variance for different time separations can be calculated for the same M-scan. Ignoring any effect of the bulk

motion on the phase variance calculation, the variances calculated for two different time separations T_1 and T_2 are given by:

$$\sigma_{\Delta\phi}^2(z, T_1) = \sigma_{\Delta\phi, \text{scatterer}}^2(z, T_1) + \sigma_{\Delta\phi, \text{SNR}}^2(z) \quad (3.39)$$

$$\sigma_{\Delta\phi}^2(z, T_2) = \sigma_{\Delta\phi, \text{scatterer}}^2(z, T_2) + \sigma_{\Delta\phi, \text{SNR}}^2(z). \quad (3.40)$$

By choosing the parameters $T_1 = \tau_0 = 40 \mu\text{s}$ and $T_2 = \beta\tau_0 = \beta(40 \mu\text{s})$ where $\beta \gg 1$, it is assumed that $\sigma_{\Delta\phi, \text{scatterer}}^2(z, T_2) \gg \sigma_{\Delta\phi, \text{scatterer}}^2(z, T_1)$. The basic phase contrast metric used for the MB-scan is chosen to be $\sigma_{\Delta\phi}^2(z, T_2) - \sigma_{\Delta\phi}^2(z, T_1)$ such that:

$$\sigma_{\Delta\phi}^2(z, T_2) - \sigma_{\Delta\phi}^2(z, T_1) \cong \sigma_{\Delta\phi, \text{scatterer}}^2(z, T_2). \quad (3.41)$$

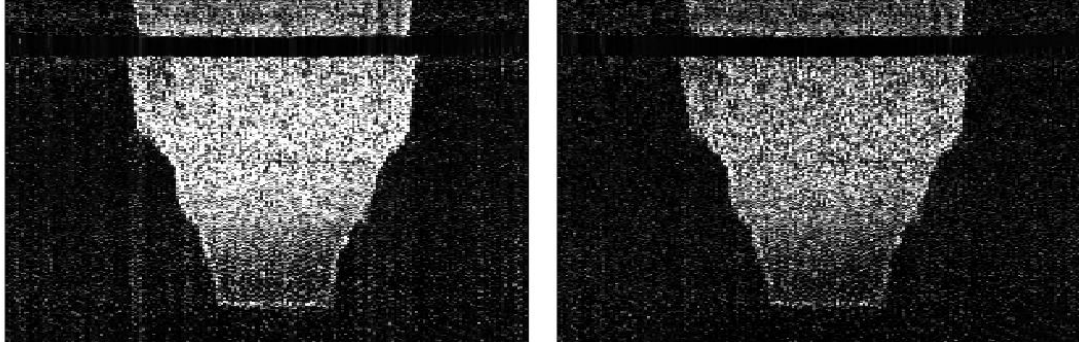


Figure 3.16 a): Phase variance contrast images for maximum phase change time separation of $T_2 = 40\tau_0 = 1.6 \text{ ms}$ (left) and $T_2 = 20\tau_0 = 800 \mu\text{s}$, (right). With M-scan acquisition times of $T_{\text{M-Scan}} = 8 \text{ ms}$ and $T_{\text{M-Scan}} = 4.8 \text{ ms}$ respectively, the total time required to acquire these contrast images is 1.6 s (left) and 0.96 s (right).

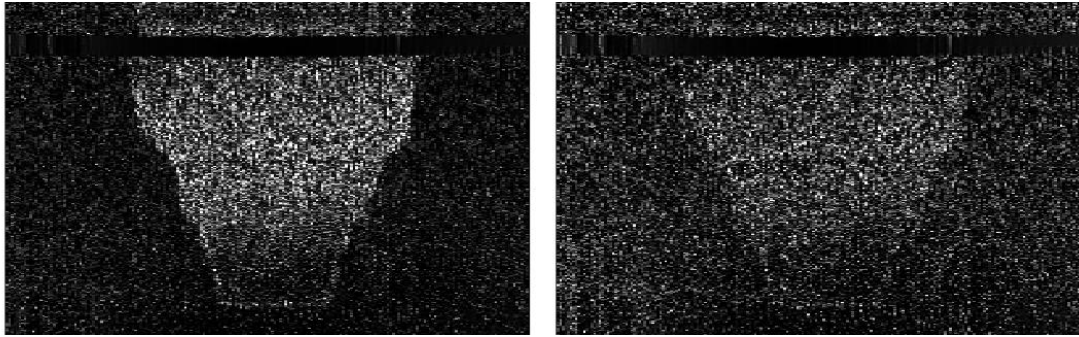


Figure 3.16 b): Phase variance contrast images for maximum phase time separation of $T_2 = 10\tau_0 = 400 \mu\text{s}$ (left) and $T_2 = 5\tau_0 = 200 \mu\text{s}$ (right). With M-scan acquisition times of $T_{\text{M-Scan}} = 2.4 \text{ ms}$ and $T_{\text{M-Scan}} = 1.2 \text{ ms}$ respectively, the total time required to acquire these images is 0.48 s (left) and 0.24 s (right).

To optimize the possible contrast for a given M-scan length and to allow for proper variance statistics, a maximum time separation for phase changes was chosen to be $T_2 = \beta\tau_0 = \beta(40 \mu\text{s})$ for an M-scan length of $T_{M\text{-Scan}} \approx 6T_2 = 6\beta(40 \mu\text{s})$. The result for a range of choices of β was plotted in Figure 3.16.

One of the major assumptions of the phase contrast image is that the SNR phase error remains constant over different time separations. The problem lies in the fact that even a small fluctuation of the phase variance calculations of the noise terms results in a non-negligible phase contrast being imaged. To further improve the phase contrast image, thresholds were applied to try and remove the effect of the noise pixels. Using phase variance contrast with $T_2 = 25\tau_0 = 1 \text{ ms}$ and statistics used from 200 A-scans, thresholds were applied based on $\sigma_{\Delta\phi}^2(z, T_1)$ or the averaged OCT intensity of the image. In the ideal case, $\sigma_{\Delta\phi}^2(z, T_1)$ contains only the SNR phase error and corresponds to the averaged OCT intensity of the image. To eliminate only the extremely noisy pixels, the upper bound threshold of $\sigma_{\Delta\phi}^2(z, T_1) = 3 \text{ radians}^2$ can be used, which is equivalent to setting a lower bound threshold on the averaged OCT intensity at the level of the mean OCT noise of the image, designated as $\langle N^2 \rangle$ previously.

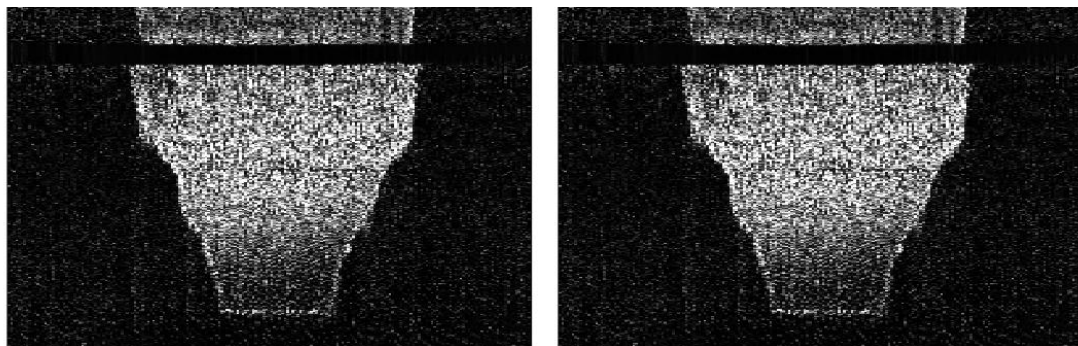


Figure 3.17 a): Phase variance contrast images for phase change time separation of $T_2 = 25\tau_0 = 1 \text{ ms}$, $T_{M\text{-Scan}} = 8 \text{ ms}$. The threshold applied to each image to reduce the noise terms are $\sigma_{\Delta\phi}^2(z, T_1) = 3 \text{ radians}^2$ (left) and OCT intensity = mean OCT noise level (right).

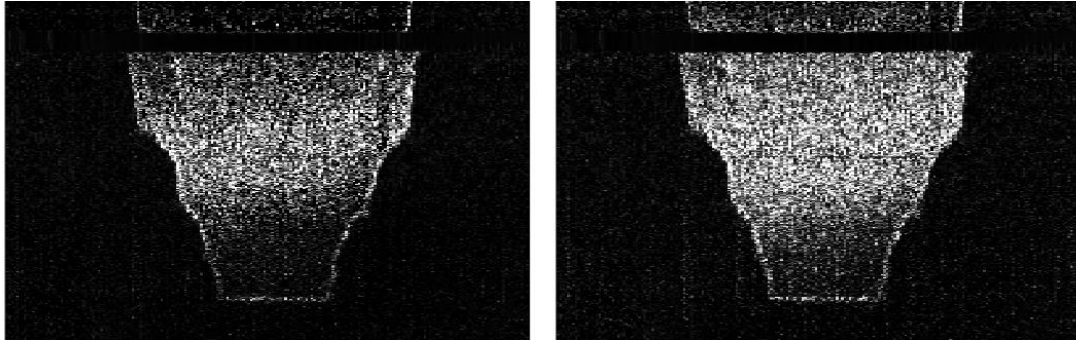


Figure 3.17 b): Phase variance contrast images for phase change time separation of $T_2 = 25\tau_0 = 1$ ms, $T_{M-Scan} = 8$ ms. The thresholds applied to each image to reduce noise terms are $\sigma^2_{\Delta\phi}(z, T_1) = 0.5$ radians² (left) and $\sigma^2_{\Delta\phi}(z, T_1) = 1$ radians² (right).

While thresholding more noise data does improve contrast in parts of the image, the sacrifice of the increased threshold is that interferometric signal near the noise level starts to become blocked by the threshold as well. This effect can be observed from the phase thresholds of $\sigma^2_{\Delta\phi}(z, T_1) = 0.5$ radians² and $\sigma^2_{\Delta\phi}(z, T_1) = 1$ radians², which corresponds to OCT signal 6 dB and 0 dB above the mean noise level respectively. The optimum threshold appears to be $\sigma^2_{\Delta\phi}(z, T_1) = 1$ radians², which corresponds to the point where SNR = 1.

The MB-scan has demonstrated the ability of using phase variance as a source of contrast not available from a single OCT intensity image. Although contrast has been demonstrated, there are serious limitations to the feasibility of using MB-scans to create 3D phase contrast imaging. The ideal phase contrast data set would be acquired within one memory buffer, limiting the effects of sample motion and alignment drift on the data acquisition. The MB-scan presented for the agarose/Intralipid sample contained a total of 40,000 A-scans, which allows for ~ 3 MB-scans of this size to be acquired within one buffer. By dropping the total acquisition time by reducing statistics so that contrast was still visible, the efficiency of the MB-scan can experience some improvement.

For the agarose/Intralipid case, phase variance contrast was still visible for the time separations of $T_2 = 10\tau_0 = 400$ μ s, requiring only 2.4 ms per M-scan of the MB-scan. With these statistics the MB-scan acquires a total of 12,000 A-scans, allowing for ~ 11 MB-scans

to be acquired within one buffer. While a 200 x 11 transverse pixel area of imaging may not be ideal for most cases, this can be adjusted to 45 x 45 transverse locations for the same phase contrast capabilities. Reducing the statistics of the MB-scan limits the observable motion with this technique. To acquire 3D phase contrast data, a different acquisition technique is required.

For 3D phase contrast imaging, the ideal acquisition would be able to (i) have large time separations between the phase measurements and (ii) acquire the entire data for a 2D phase contrast image in a minimum amount of time.

3.5 Phase Contrast Method: BM-Scan

To improve the efficiency of the data collection, a different approach is required to the transverse scan pattern during acquisition. The MB-scan presented earlier acquires data by moving to each transverse location and waiting until enough phase information has been acquired before moving onto the next position. A large portion of the acquisition with this method is wasted simply waiting for the motion of the scatterers to surpass the accuracy limitations of the measurement. Instead of waiting at one location acquiring information, acquisition efficiency can be improved by taking a single phase measurement at each of the transverse locations before returning to the original location to repeat the phase measurements.

Rather than acquiring successive A-scans while waiting at one transverse location, A-scans can be acquired while scanning across the sample. When the scan beam returns to the original location to acquire the next phase measurement, a large time separation has occurred which is ideal for phase variance contrast measurements. By repeating this measurement for enough statistics to calculate the phase variance, the 2D phase contrast image can be determined. The process of measuring multiple B-scans over time for the same transverse scan region will be referred to as a BM-scan.

The BM-scan is a very efficient method of acquiring 2D phase contrast image data. The minimum time between phase measurements is determined by the acquisition speed of the spectrometer τ_0 , the number of transverse pixels used in the B-scan and the speed capabilities of the transverse scanner in the system. To ensure a constant time separation of phase measurements across the entire image, only phases measured during one scan direction along the primary transverse scan axis will be used in phase variance calculations. With this constraint and the continuous acquisition of spectrometer data, all the data acquired during the fly-back of the transverse scan wastes space in the memory buffer.

Using the same terminology as used previously in Chapter 3.2, the total number of spectrometer acquisitions which are acquired in one cycle of the transverse scan is N_X . The percentage of spectrometer measurements which occur during the primary transverse scan which creates the B-scan was X_{DUTY} . The number of A-scans which compose each B-scan of the BM-scan is given by:

$$N_{XSCAN} = X_{DUTY} N_X. \quad (3.42)$$

This leads to a time separation between the phase measurements and successive B-scans within the BM-scan of $T = N_X \tau_0$.

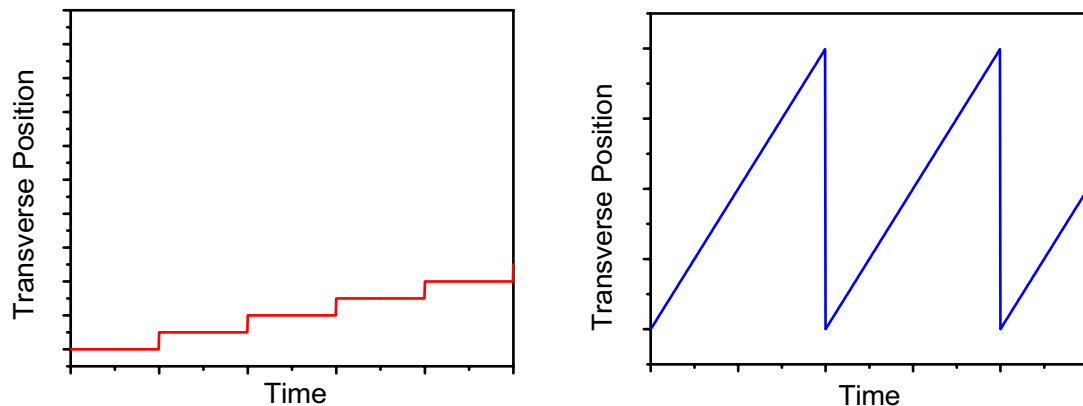


Figure 3.18: Schematic of transverse scan patterns for MB-scan (left) and BM-scan (right).

Phase contrast for an MB-scan is calculated using the difference between the phase variance calculated for successive A-scans and the variance for phase changes with much larger time separations. This method achieves motion contrast because the dominant source of phase noise in the successive A-scan phase change is the SNR-limited phase error. To achieve phase contrast for a BM-scan, the phase changes between successive A-scans can no longer be considered a good approximation of the SNR phase error. The transverse scan between successive A-scans in this method induces additional phase errors, as described in Chapter 3.3.4. Numerical estimates of the phase noise based on the averaged OCT intensity are an excellent alternative to allow creation of a phase variance contrast image.

Using an MB-scan, phase error is calculated from phase changes of all depths of the successive A-scan measurements of a stationary paper sample. The variance of the phase changes is compared against the averaged OCT intensity, to compare against the theoretical prediction of equation (3.21). By fitting the phase error data which occurs at intensities approximately 10–25 dB above the noise level of the system to the expected form of the SNR-limited phase noise, the mean OCT noise level $\langle N^2 \rangle$ was determined. The measured OCT intensity I^2 is a combination of the interferometric signal S^2 and the noise signal N^2 such that the averaged OCT intensity is of the form:

$$\langle |\tilde{I}|^2 \rangle = S^2 + \langle N^2 \rangle. \quad (3.43)$$

With the mean OCT noise level determined, the interferometric signal can be extracted from the measured OCT intensity. The measured SNR-limited phase noise is plotted against the interferometer signal, normalized to the mean OCT noise level. Phase error is calculated as a function of normalized OCT interferometer signal data. Noise estimation (red line) is performed by fitting data in the 10 dB to 25 dB range to the expected form of SNR-limited phase error.

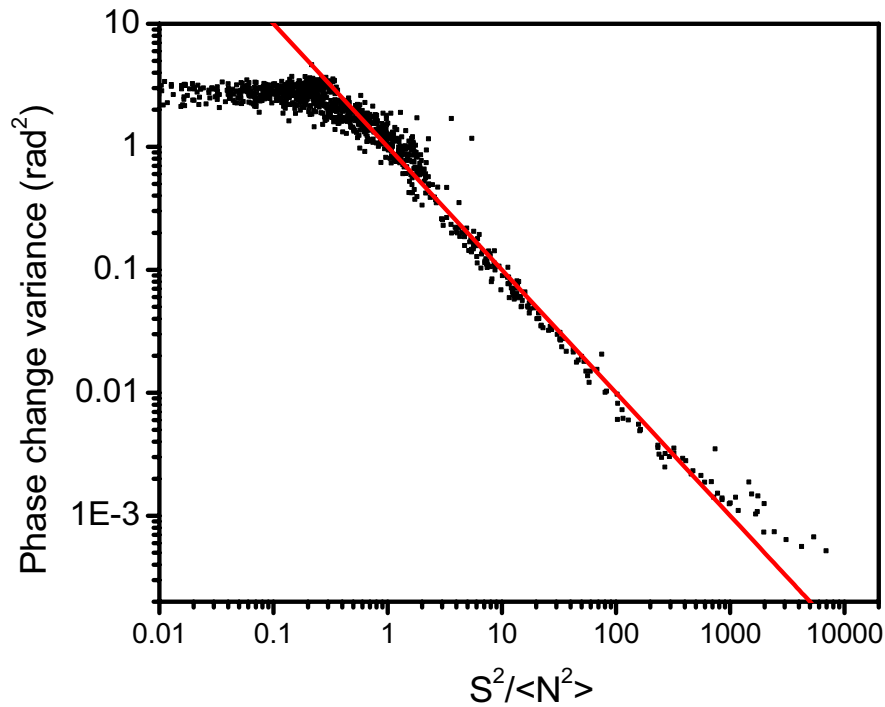


Figure 3.19: SNR-limited phase noise plotted versus averaged OCT intensity signal.

The expected form of the SNR-limited phase noise deviates from the measured values at very low and very high cases of $S^2/\langle N^2 \rangle$. For $S^2/\langle N^2 \rangle \sim 1$, this discrepancy is most likely caused by the statistical variations of the noise, limiting the calculation of the interferometric signal. The measured phase error reaches a maximum level at approximately 3 radians², which is caused by the imposed limitations of maximum phase changes between $-\pi$ and $+\pi$. For a completely random distribution of phase changes between $-\pi$ and $+\pi$, the standard deviation is approximately 1.8 radians. This limits the expected maximum phase variance measured for a purely noise situation to approximately 3.2 radians². For the very high $S^2/\langle N^2 \rangle$ case, the expected phase error is small enough that other sources of error can dominate. In this case, the limiting phase error is due to the bulk motion between the system and the sample during the acquisition of this phase data.

3.5.1 Varying BM-Scan Imaging Parameters

The BM-scan acquired data for the agarose/Intralipid sample used for the MB-scan, utilizing the same imaging parameters in this case. The BM-scan is composed of 200 transverse locations extending over 1.6 mm. All of the images presented are scaled to the appropriate dimensions. In the demonstrated BM-scan, the time between phase measurements, defined by the B-scan time and the fly-back time, is $T = 10$ ms. With 200 transverse pixels acquired at $40 \mu\text{s}$ each, this defines the x-scan duty cycle at $X_{\text{DUTY}}=0.8$.

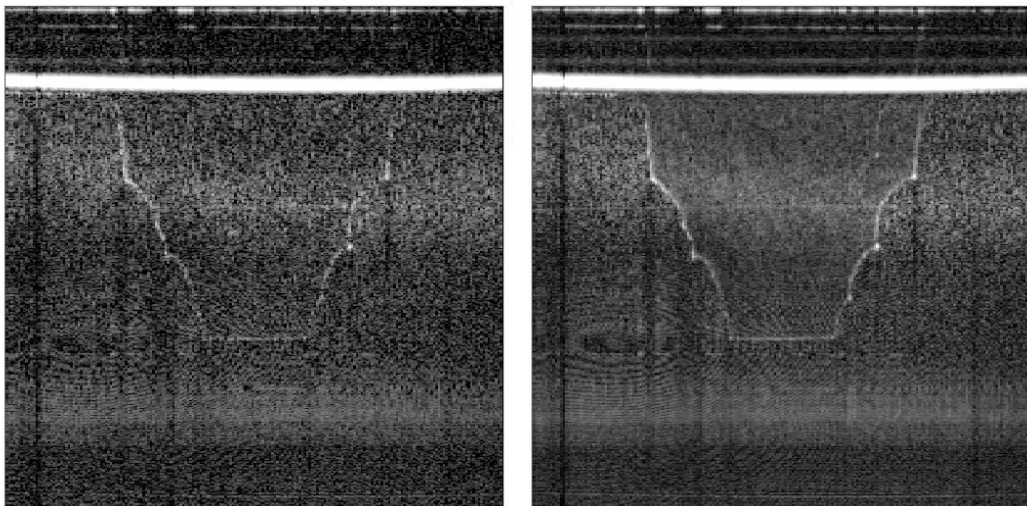


Figure 3.20: OCT intensity images of 2% agarose well filled with an 0.1% Intralipid solution for no averaging (left) and averaging over 5 sequential B-scans (right)

The intensity images created with the BM-scan are comparable to the case of the MB-scan. The B-scan containing no averaging still has limited contrast between the agarose and Intralipid regions, while contrast can be observed in the averaged image.

The phase variance imaging parameters for the BM-scan are slightly different than those of the MB-scan. The time between phase measurements for this BM-scan is $T = 10$ ms, with no flexibility available to alter this value after the data has been acquired. Choosing a different time separation in parameter space requires a different BM-scan acquisition pattern. The time separation for this BM-scan is more than six times larger than the longest

time separation used in the MB-scan presented earlier in Figure 3.17, which is expected to result in larger measured phase variances. The image scale for the phase variance images ranges from 0 to 3 radians². The main difference in the variance images is the implementation of a bulk motion removal algorithm, to reduce the effect relative motion between the sample and the system has on phase measurements.

A weighted mean technique was used to calculate the bulk motion, utilizing phase changes from all depths within a chosen region of the A-scan. Each phase change calculated was weighted by the intensity of the OCT signal for that depth to reduce the effect SNR-limited phase error $\sigma_{\Delta\phi, \text{SNR}}(z)$ has on the calculation of the bulk motion removal. For phase measurements separated by time T , the bulk axial motion is calculated as:

$$\Delta\phi_{\text{bulk}}(T) = \frac{\sum_z [I(z)\Delta\phi(z, T)]}{\sum_z [I(z)]}. \quad (3.44)$$

The signal amplitude $I(z)$ is the linear form of the OCT intensity $I^2(z)$, which is imaged in the form of $20 \log(I(z))$. The z summation for this equation is over a chosen depth region of the A-scan which contains the sample reflections. The phase changes $\Delta\phi(z, T)$ used were conditioned to limit phase changes between $-\pi$ and $+\pi$ to avoid phase wrapping issues. With this method of bulk phase removal from the entire depth sample reflections, the accuracy of this method becomes limited to approximately the SNR-limited phase error of the strongest sample reflection in the entire depth. This places an expected lower limit on identifiable phase changes after compensating for the other effects.

Before implementing the numerical phase noise removal, the phase variance image was plotted using 5 and 16 phase measurements to calculate the variance. With the parameters used in the BM-scan, the total imaging time for each of these images is 50ms and 0.16s respectively. These images demonstrate similar contrast to the largest time separations of the phase variance contrast images of the MB-scan in Figure 3.17.

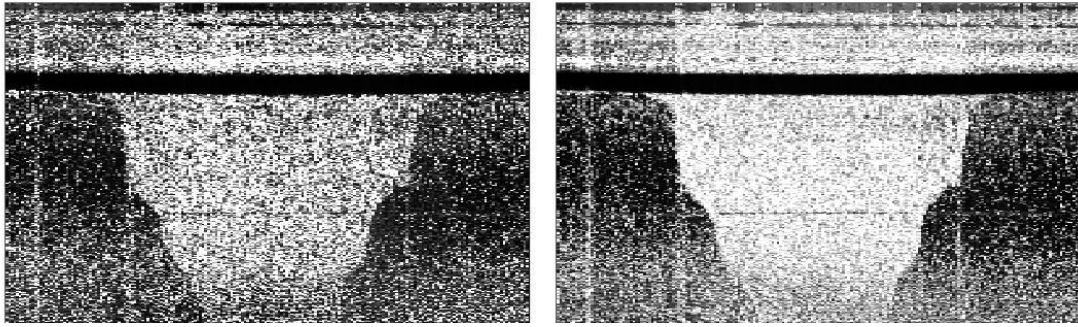


Figure 3.21: BM-scan phase variance images without thresholds or phase error removal. The total number of B-scans used to create the image is 5 (left) and 16 (right), requiring a total acquisition time for the image data of 50 ms (left) and 0.16 s (right).

The phase variance contrast images incorporate the removal of the numerically estimated phase error as well as a threshold on the phase data based on the averaged OCT intensity signal. The threshold used for the phase contrast images was the case where $SNR=1$ (where the measured OCT intensity equaled twice the mean OCT noise level). The two images presented demonstrate again the cases of 5 and 16 total B-scans to create the phase variance.

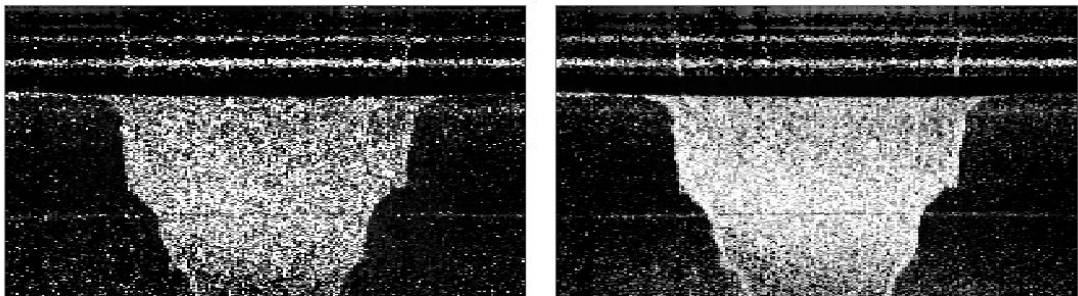


Figure 3.22: BM-scan phase variance contrast images with SNR-limited phase error removed and thresholds applied based on the intensity image. The total number of B-scans used to create the image is 5 (left) and 16 (right), requiring a total acquisition time for the image data of 50 ms (left) and 0.16 s (right).

To optimize the buffer acquisition with multiple BM-scans, the minimum number of statistics possible must be determined. For total of 5 B-scans used in a BM-scan results in a total of 4 phase changes calculated at a given location. Fewer than 5 B-scans would not produce enough statistics to properly calculate the variance of the phase changes.

There are several options available to improve the phase variance image contrast for a given BM-scan of fixed statistics. An overestimate of the phase error that is removed from the image would reduce the effects of noise terms that are not removed completely due to limited statistics in the calculation. A very useful tool for improving contrast is image filtering. Median filters were applied to the phase variance contrast image in the case of 5 B-scans, where the statistics are limited. A median filter of rank ζ for a given direction analyzes a given pixel and ζ pixels on each side of it, calculating the median of the group and replacing the value into the pixel location. This filter is very useful in reducing highly localized noise, like the cases found in the phase contrast images. Due to the oversampling in the axial direction of the image due to the spectrometer and the coherence length, a median filter of rank 2 was applied axially to the contrast image along with a median filter of rank 1 which was applied transversely.

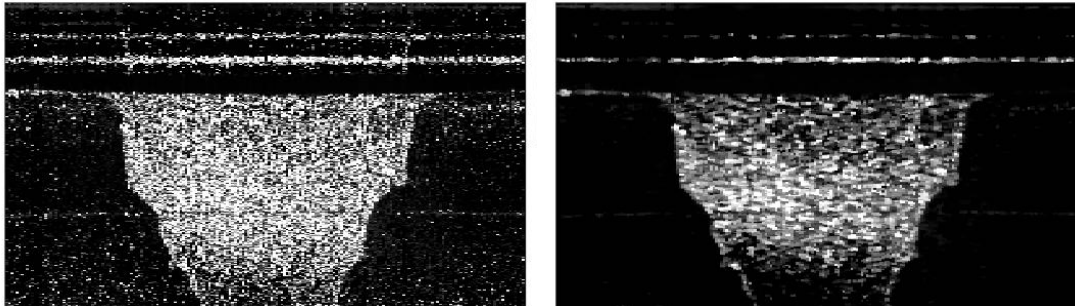


Figure 3.23: BM-scan phase variance contrast image for 5 total B-scans used. The right image applied a median filter of rank 2 axially (5 pixels) and rank 1 (3 pixels) transversely. Total time for both images is 50 ms.

After the filtering was applied to the image, there was a clear reduction of the noise in the image. The horizontal lines visible on the contrast image correspond to spectrometer noise that is very difficult to eliminate in general, of a form which differs between various CCD cameras. While the contrast of the Intralipid solution appears to have suffered slightly due to the filtering, this approach can be very useful to reduce OCT noise effects on phase contrast images.

To demonstrate the importance of bulk motion removal, the phase variance contrast image was re-analyzed with and without bulk motion removal. The images were not cropped like

the previous images to also demonstrate a limitation to bulk motion removal in scenarios where mirror terms appear in the image. In the first image containing no bulk motion removal, the large line corresponding to the air/water interface is expected to have no variance measured if no motion was occurring in the system, which is not the case here.

With the bulk motion removal, many portions of the phase contrast image which are expected to be static reduce in intensity. But there is a broad reflection at the bottom of the image which observes an increase in phase contrast after removal. From a static B-scan image, it is difficult to identify mirror term reflections which can limit the performance of a phase contrast image.

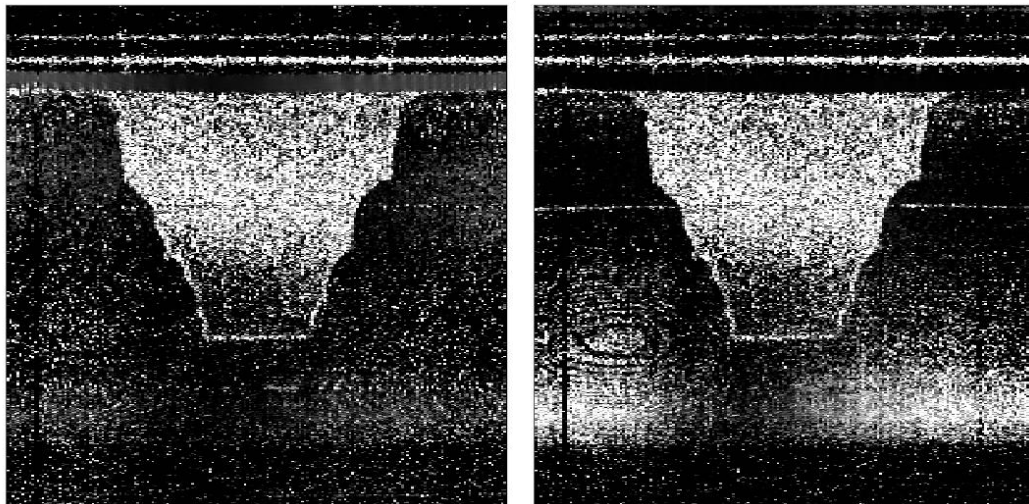


Figure 3.24 a): BM-scan phase variance contrast image for cases of no phase removal (left) and standard bulk phase removal method (right).

One option to deal with mirror terms present within a phase contrast image is to calculate the phase variance contrast for multiple cases and choose the minimum value as the image pixel value. By choosing the minimum value between the bulk removal contrast and the phase contrast without any removal, the result is the expected minimum of the previous two images. To properly remove the effect of the mirror terms, the contrast image should be the minimum between the bulk removal contrast image and the bulk addition contrast image, where the calculated bulk motion is added to the image to reduce only the contrast from the mirror terms. This method does remove the mirror term bulk motion effects while only

slightly affecting the contrast measured from the Intralipid solution by canceling out some scatterer motion in the cases where it was in the opposite direction to the bulk motion experienced.

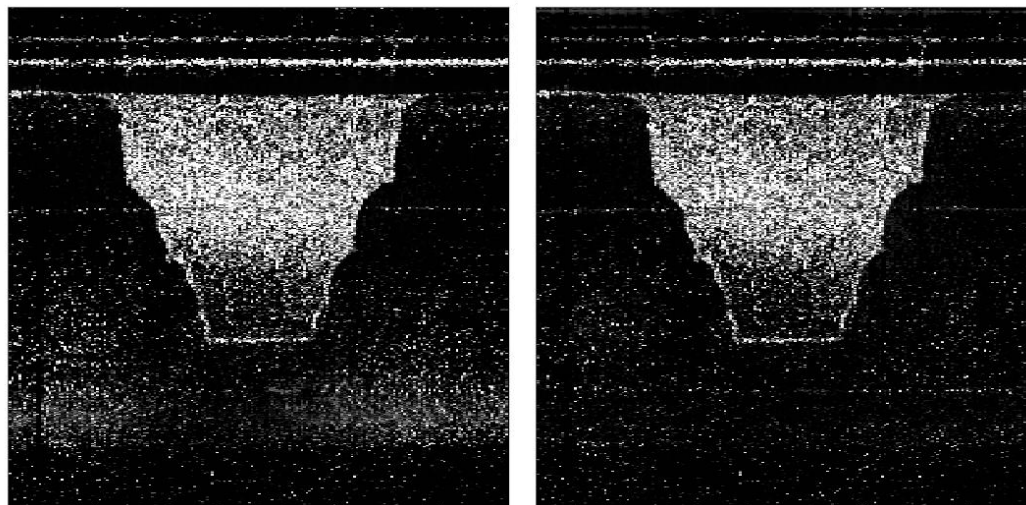


Figure 3.24 b): BM-scan phase variance contrast image calculated from the minimum of the cases of no phase removal versus bulk phase removal (left) and the minimum of the cases of bulk phase removal method and bulk phase addition method (right).

The BM-scan in its current configuration is ideal for 3D phase contrast imaging in one buffered acquisition. With the maximum possible computer memory buffer, a transverse scan area of 200 x 100 pixels is possible using the BM-scan with statistics limited to only 5 B-scans total. There is a lot of imaging potential for this method once all of the limits are understood.

The contrast methods developed in this chapter have demonstrated motion contrast in a sample without any induced flow. To fully understand the capabilities of these techniques to observe motion contrast, the next step is to use a living sample which will produce flow contrast to be evaluated.

3.6 References

1. "Gaussian beam," Wikipedia, http://en.wikipedia.org/wiki/Beam_waist.
2. "Numerical aperture," Wikipedia, http://en.wikipedia.org/wiki/Numerical_aperture.
3. J.W. Goodman, Introduction to Fourier Optics, 1st ed. (McGraw-Hill, 1968).
4. M. Born and E. Wolf, Principles of Optics; Electromagnetic Theory of Propagation, Interference and Diffraction of Light, (Pergamon Press, 1959).
5. W. Drexler, "Ultrahigh-resolution optical coherence tomography," J. Biomed. Opt. 9, 47 (2004).
6. W. Drexler et al., "Enhanced Visualization of Macular Pathology with the use of Ultrahigh-Resolution Optical Coherence Tomography," Arch. Ophthalmol. 121, 695 (2003).
7. SuperLum Diodes Ltd., www.superlumdiodes.com.
8. American National Standards Institute-ANSI, www.ansi.org.
9. S.H. Yun et al., "Motion Artifacts in OCT with Frequency Domain Ranging," Opt. Express 12, 2977 (2004), <http://www.opticsexpress.org/abstract.cfm?id=80320>.
10. S. Yazdanfar et al., "Frequency estimation precision in Doppler optical coherence tomography using the Cramer-Rao lower bound," Opt. Express 13, 410 (2005), <http://www.opticsexpress.org/abstract.cfm?id=82377>.
11. B. Vakoc et al., "Phase-resolved optical frequency domain imaging," Opt. Express 13, 5483 (2005), <http://www.opticsexpress.org/abstract.cfm?id=84914>.
12. B.R. White et al., "In vivo dynamic human retinal blood flow imaging using ultra-high-speed spectral domain optical coherence tomography," Opt. Express 11, 3490 (2003), <http://www.opticsexpress.org/abstract.cfm?id=78206>.
13. R.A. Leitgeb et al., "Real-time measurement of in vitro flow by Fourier-domain color Doppler optical coherence tomography," Opt. Letters 29, 171 (2004).
14. B. Park et al., "Real-time fiber-based multi-functional spectral-domain optical coherence tomography at 1.3 μm ," Opt. Express 13, 3931 (2005), <http://www.opticsexpress.org/abstract.cfm?id=84093>.
15. R.K. Pathria, Statistical Mechanics, 2nd ed. (Butterworth, 2001).
16. K.W. Gossage et al., "Texture analysis of optical coherence tomography images: feasibility for tissue classification," J. Biomed. Opt. 8, 570 (2003).